On the Mechanisms Driving Latent Heat Flux Variations in the Northwest Tropical Atlantic

Pablo Fernández[1], Sabrina Speich[1], Hugo Bellenger[1], Diego Lange Vega[2], Johannes Karstensen[3], Dongxiao Zhang[4], Cesar Barbedo Rocha[5]

[1]Laboratoire de Météorologie Dynamique, École Normale Supérieure, Department of Geosciences, Paris, France.
[2]University of Hohenheim, Institute of Physics and Meteorology, Stuttgart, Germany.
[3]GEOMAR Helmholtz Centre for Ocean Research, Kiel, Germany.
[4]CICOES/University of Washington and NOAA Pacific Marine Environmental Laboratory, Seattle, USA.
[5]Instituto Oceanográfico, Universidade de São Paulo, São Paulo, Brazil.

Key Points:

- Latent heat flux (LHF) presents strong spatial variations in the northwest tropical Atlantic (NWTA), which has a complex ocean circulation.
- Surface winds and sea surface temperature are the major drivers of LHF changes. The Amazon plume remains as a second-order contributor.
- It is necessary to distinguish between spatial scales (mesoscale and below versus large-scale) when assessing the ocean's influence on LHF.

Corresponding author: Pablo Fernández, pablo.fernandez@lmd.ipsl.fr

Abstract

The Northwest Tropical Atlantic (NWTA) is a region with complex surface ocean circulation. The most prominent feature is the North Brazil Current (NBC) and its retroflection at 8ºN that leads to the formation of numerous mesoscale eddies known as NBC rings. The NWTA also receives the outflow of the Amazon River, generating freshwater plumes that can extend up to 100,000 km^2. These two processes affect the spatial variability of the region's surface latent heat flux (LHF). First, the presence of surface freshwater modifies the vertical stratification of the ocean limiting the amount of heat that can be released to the atmosphere. Second, they create a highly heterogeneous mesoscale sea-surface temperature (SST) field that directly influences near-surface atmospheric circulation. These effects are illustrated by observations from the ElUcidating the RolE of Cloud-Circulation Coupling in ClimAte - Ocean Atmosphere (EUREC^{4}A-OA) and Atlantic Tradewind Ocean-Atmosphere Interaction Campaign (ATOMIC) experiments, satellite and reanalysis data. We decompose the LHF budget into several terms controlled by different atmospheric and oceanic processes to identify the mechanisms leading to LHF changes. We find LHF variations of up to 160 W m^2, of which 100 W m^2 are associated with wind speed changes and 40 W m^2 with SST variations. Surface currents or stratification-change associated heat release remain as second-order contributions with LHF variations of less than 10 W m^2 each. Although this study is limited by the paucity of collocated observations, it highlights the importance of considering these three components to properly characterize LHF variability at different spatial scales.

Plain Language Summary

The Northwest Tropical Atlantic (NWTA) is a region with a complex ocean circulation. It is dominated by the North Brazil Current (NBC), which parallel to the South American coast and changes its direction at 8ºN. This leads to the formation of closed swirling circulations known as NBC rings. The NWTA also receives the outflow of the Amazon River. These two features affect the heat exchange between the ocean and the atmosphere associated with water evaporation (latent heat flux, LHF) as they modify sea surface temperature, salinity and the near-surface atmospheric circulation. Here, we use the observations collected from the ElUcidating the RolE of Cloud-Circulation Coupling in ClimAte - Ocean Atmosphere (EUREC^{4}A-OA) and Atlantic Tradewind Ocean-Atmosphere Interaction Campaign (ATOMIC) experiments, satellite data and combined observations with models to identify the key mechanisms leading to such LHF variations. More of 60% of them are associated to surface winds whilst sea surface temperature is behind a 25%. The Amazon outflow accounts for less than 10%. Although this study is limited by the paucity of oceanic, atmospheric and air-sea interface observations located at the same point in time and space, it highlights the importance of considering these three components to properly describe LHF variability.

1 Introduction

The Northwest Tropical Atlantic (NWTA) near the mouth of the Amazon River is a region of complex surface ocean dynamics (Fig. 1a, the black box delineating the NWTA) at the transition between equatorial and subtropical waters. The most prominent feature is the North Brazil Current (NBC), which flows northward parallel to the South American coast. The NBC retroflects at about 8 °N and forms the North Equatorial Countercurrent. The NBC current system is closely connected to two important oceanic features: the Amazon River freshwater plume (Reverdin et al., 2021) and NBC rings (Johns et al., 1990; Richardson et al., 1994).

The Amazon is the world's most powerful river system, accounting for half of the total Atlantic river discharge (Gévaudan et al., 2021) and one fifth of the global river freshwater input to the ocean (Dai & Trenberth, 2002). The extension of the Amazon River

discharge, although minimal between January and March (Fournier et al., 2015), creates strong spatial heterogeneity in the sea surface salinity (SSS) field (Fig. 1a), which also affects upper ocean temperatures. Indeed, SSS can affect SST through its influence on the upper ocean stratification. When salinity dominates ocean stratification, the ocean layer in direct contact with the atmosphere which is named the mixed layer (ML), becomes thinner. This situation favors the formation of the so-called barrier layers (BLs) at the base of the ML which might support the development of a temperature inversion (Anderson et al., 1996; de Boyer Montégut et al., 2007; Foltz & McPhaden, 2009; Vialard & Delecluse, 1998; Mignot et al., 2012; Mahadevan et al., 2016; Krishnamohan et al., 2019). In case of an established BL, heat and momentum inputs are often limited to the shallow ML which reacts quicker to the atmospheric forcing and cools (warms) more rapidly in winter (summer) as a consequence of the inhibition (enhancement) of the interaction with the deeper ocean (Miller, 1976; Sprintall & Tomczak, 1992). This leads to negative (positive) SST anomalies relative to their environment over the Amazon River plume and hence to reduced (increased) air-sea heat fluxes. However, the importance of this response is still debated, as observational studies suggest a strong impact (Pailler et al., 1999; Foltz & McPhaden, 2009) of BLs on SST, which models do not seem to reproduce (Breugem et al., 2008; Balaguru et al., 2012; Hernandez et al., 2016).

The shape and extent of the Amazon River plume is often modified by the local circulation induced by the NBC rings (Reverdin et al., 2021; Olivier et al., 2022) and Fig. 1a. They form at the NBC retroflection and move northwest towards the Lesser Antilles where they coalesce and dissipate due to their interaction with the complex topography (Fratantoni & Richardson, 2006; Jochumsen et al., 2010; Andrade-Canto & Beron-Vera, 2022; Subirade et al., 2023) and Fig. 1b. These eddies can modify the SST and SSS fields in the region in two different ways: by transporting the water trapped in their core during their formation (eddy trapping) and/or by stirring the surrounding waters, inducing the formation of cross-slope filaments that further cascade into smaller submesoscale structures (eddy stirring) (Olivier et al., 2022; Subirade et al., 2023). The NBC rings are characterized by a mean radius of 200 km (Fratantoni & Richardson, 2006), a vertical extent that varies between 200-300 m to 1000 m (Fratantoni & Richardson, 2006; Fratantoni & Glickson, 2002; Johns et al., 2003), azimuthal velocities between 0. 1 to 0.17 m s^{-1} and a northwestward mean translation velocity between 8 and 15 km day^{-1} (Fratantoni & Richardson, 2006; Johns et al., 2003; Garraffo et al., 2003; Didden & Schott, 1993; Jochumsen et al., 2010). The NBC rings play an essential role in the interhemispheric transport of mass, heat, salt, and biogeochemical properties of the ocean, and thus make an important contribution to the Atlantic Meridional Overturning Circulation (Johns et al., 2003). While most studies of the rings have focused on their biogeochemical and/or physical properties (Olivier et al., 2022; Subirade et al., 2023), little has been done regarding their impact on air-sea heat fluxes and, in particular, on the latent heat flux (LHF).

There is considerable evidence in the literature that SST gradients at the mesoscale (O(10-200) km) modify the lower atmosphere and hence air-sea heat fluxes (Bishop et al., 2017; Acquistapace et al., 2022). There are two documented mechanisms that drive such modifications: the downward momentum mixing (DMM) mechanism (Hayes et al., 1989; Wallace et al., 1989) and the pressure adjustment (PA) mechanism (Lindzen & Nigam, 1987). In the DMM mechanism, the presence of warm SST anomalies destabilizes the marine atmospheric boundary layer (MABL) and enhances vertical motion. This fact favors the entrainment of drier air from the free troposphere into the MABL, thereby increasing the near-surface wind speed. In turn, the PA mechanism states that surface wind convergence (divergence) is generated over SST maxima (minima) as the warm (cold) SST patches generate surface pressure lows (highs).

The effect of these two mechanisms is documented from hourly to weekly time scales in several parts of the world ocean. For example, Frenger et al. (2013) show that mesoscale eddies control the atmospheric response in terms of winds, clouds, and precipitation via

the DMM mechanism on weekly time scales in the Southern Ocean. A similar result has been obtained in the Gulf Stream region (Minobe et al., 2008), the Kuroshio extension (Xu et al., 2011; J. Ma et al., 2015; L. Chen et al., 2017), in the South China Sea (H. Liu et al., 2018; Y. Liu et al., 2020), and in the Agulhas (O'Neill et al., 2005) and Malvinas (Villas Bôas et al., 2015; Leyba et al., 2017) currents. In addition, there is evidence that the submesoscale (O(1-10) km) SST gradients can also influence the surface wind response (Meroni et al., 2018; Gaube et al., 2019), generating LHF values significantly larger than the state-of-the-art parameterizations would suggest (Shao et al., 2019). In turn, PA has been shown to influence clouds and precipitation in the cold wakes of tropical cyclones (Z. Ma et al., 2020) through a cross-track secondary circulation (Pasquero et al., 2021).

The relative importance of DMM and PA in the northwest tropical Atlantic in modifying the LHF has been assessed by Fernández et al. (2023) using satellite data. In this region, LHF gradients of more than 50 W m^{-2} are observed, an amount that accounts for more than 40% of the climatology (Fig. 1b). They find that DMM largely dominates over PA when the small-scale (features of less than 150 km) SST-near-surface-atmosphere interactions are considered. If the total increase in LHF per °C of SST is about 33 % of the climatology, 28 % is due solely to the changes in winds and specific humidity from the MABL thickening (dynamic contribution) and the remaining 5 % is due to the fact that warmer air is able to hold more moisture (thermodynamic contribution).

Thus, the DMM provides the "top-down" physical mechanism by which the mesoscale SST affects the near-surface atmosphere, a process known as the thermal feedback (TFB) (Renault et al., 2019). However, surface ocean currents also influence surface stress and wind in a "bottom-up" process known as the current feedback (CFB) (Bye, 1985; Chelton et al., 2001). A surface current anomaly with the same (opposite) direction as the surface wind speed creates a negative (positive) relative wind anomaly, thereby decreasing (increasing) LHF (Renault et al., 2016; Takatama & Schneider, 2017). Thus, statistically, the CFB does not have a systematic effect on the near-surface wind magnitude, as a current anomaly can induce a positive or negative wind anomaly depending on the relative orientation of the surface current to the surface wind.

The purpose of this study is to quantify how all the processes described in the previous sections affect the LHF in the NWTA during winter. To this end, we make use of the *in-situ* observations collected during the EUREC^{4}A-OA (ElUcidating the RolE of Cloud-Circulation Coupling in ClimAte -Ocean Atmosphere `www.eurec4a.eu`) and Atlantic Tradewind Ocean-Atmosphere Mesoscale Interaction Campaign (ATOMIC) field experiment (Stevens et al., 2021; Subirade et al., 2023). Aiming to improve the understanding of the interplay between clouds and shallow convection in the atmosphere, as well as small-scale air-sea interactions in the NWTA (and their role in climate), EUREC^{4}A-OA and ATOMIC took place between the 12^{th} of January and the 23^{rd} of February 2020. Unprecedented, high-resolution observational data were collected using cutting-edge technology on aircraft, ships, autonomous vehicles, and the Barbados Cloud Observatory time series (Stevens et al., 2021; Quinn et al., 2021; Karstensen et al., 2020; Speich, 2021). A wide range of innovative and standard observing platforms were deployed, including Saildrones, ocean gliders, wave gliders, surface buoys, profiling floats, and 4 research vessels (RVs). The paper is organized as follows. The data sources are presented in section 2. The different methods used to analyze the upper ocean, the air-sea interface and the vertical profiles of the atmosphere are described in section 3, and a discussion of the main results is given in section 4. A conclusion follows in section 5.

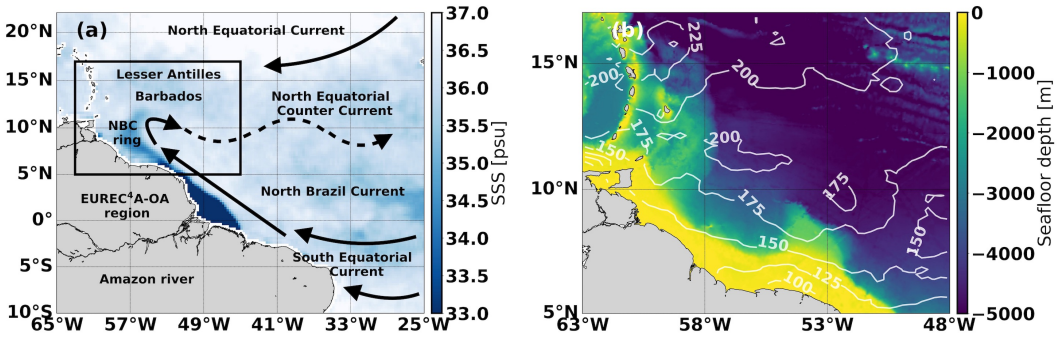

Figure 1. (a) Major dynamic features of the western equatorial Atlantic (arrows) superimposed on the SSS field averaged between 17^{th} and 19^{th} February 2020. The SSS field comes from the 4.0 version SMAP-SSS level 3, 8-day running mean gridded product (Meissner et al., 2019). The black box delineates what is referred to in the main text as the NWTA, the region where all the observations used in this article were measured. (b) Zoom in on the NWTA, the contours represent the mean February 2008-2018 LHF from SeaFlux (Clayson et al., 2014) and the shading shows the seafloor depth from the ETOPO2 product (Ducet et al., 2000). Detailed information on all datasets in this figure can be found in the section 2.

2 Data

2.1 *In-situ* Data

The EUREC^{4}A-OA/ATOMIC campaigns involved the participation of four RVs: RV *Atalante* from France (Speich, 2021), RV *Maria Sybilla Merian* hereafter referred to as *Merian* from Germany (Karstensen et al., 2020), RV *Meteor* from Germany (Mohr et al., 2020), and RV *Ronald Harmon Brown* hereafter referred to as *Ron Brown* from the United States (Quinn et al., 2021). These cruises provided numerous *in-situ* measurements of the vertical structure of the ocean and atmosphere as well as the air-sea interface.

To study the vertical structure of the ocean in the NWTA, we use the vertical profiles of temperature, salinity and density from all sampling devices launched from the four RVs: CTDs; underway CTDs (uCTDs) (only from *Atalante*, *Merian* and *Meteor*), moving vessel profilers (MVP) (from *Atalante* and *Merian*), Argo profiling float measurements, a number of underwater electric gliders (Kraken, IFM03, IFM09, IFM12, SG579, SG620 and SG637) (Subirade et al., 2023; Stevens et al., 2021; Speich, 2021; Karstensen et al., 2020; Quinn et al., 2021). We remove the vertical profiles from which the salinity and/or temperature value closest to the surface are missing. We consider these values to be the SSS and SST and we need them in order to associate each profile to a water mass as detailed below. After this operation, we are left with 1141 profiles in the NWTA with a vertical resolution of 0.5 m depth between January 17, 2020 and February 16, 2020. Special emphasis is placed on the 736 *Atalante* MVP vertical profiles sampled between the 2^{nd} and the 5^{th} of February 2020.

RV *Atalante* and RV *Merian* also provided many ship-based surface measurements. In particular, we use the air-sea interface measurements from the *Atalante* mast. Again, we focus on the mast data starting on 2^{nd} February 2020 and ending on 5^{th} February 2020. They are provided at 1 second time resolution, although all data are averaged over 10 minute intervals prior to all calculations to smooth out ship motion. The variables used include air pressure, relative humidity, air temperature and horizontal wind speed measured by the Vaisala WTX 520 weather station at 16 m for temperature and humid-

ity and 17 m for wind speed. To compute the radiative forcing at the surface, we also use the net shortwave and longwave radiation fluxes provided by the Campbell CNR4 pyranometer and pyrgeometer installed on the mast. In addition, we exploit the SST-SSS values provided by the Seacat SBE21 thermosalinograph (TSG) at 5 m depth installed on the *Atalante*, and the the X-band radar derived surface currents from the *Merian* between the 2^{nd} and the 5^{th} of February. We collocate both measurements with the *Atalante* meteorological mast to compute air-sea fluxes as described in section 1 of the Appendix.

Between the 2^{nd} and the 5^{th} of February 2020, 60 radiosondes (RS) were launched from the *Atalante* (Stephan et al., 2021). The RSs use water vapor mixing ratio (WVMR), pressure, relative humidity, air temperature, wind direction, wind speed, specific humidity, altitude, potential temperature. Each RS is associated with the nearest SST-SSS SBE21 TSG pair as described in section 1 of the Appendix. In addition, the Atmospheric Raman Temperature and Humidity Sounder (ARTHUS, Lange et al. (2019)) and two Doppler lidars (DLs, Pearson et al. (2009)) from the University of Hohenheim were deployed and operated from the *Merian* between January 25, 2020 and February 18, 2020. In this study we focus only on the vertical profiles between the 2^{nd} and the 5^{th} of February 2020 and use the low-resolution data version with averaged vertical profiles every 10 minutes, which allows us to filter out possible effects of ship motion. From ARTHUS we take the backscatter ratio (BR), air temperature and WVMR vertical profiles, which we then convert to specific humidity. From the DLs we take the horizontal and vertical wind speed vertical profiles. Note that while ARTHUS provides data from 225 m to 3025 m with 50 m spacing between levels, the vertical profiles from the DLs contain 56 vertical levels between 250 m and 3000 m with 50 m spacing. To resolve this mismatch, we perform a linear interpolation from the ARTHUS vertical resolution to the DLs vertical resolution (or a near-neighbor approximation if no data are available in the corresponding height level). Like before, we associate an SST-SSS pair from the *Merian* SBE38 TSG to each vertical profile.

This study also benefits from the unprecedented view of the upper ocean at the air-sea interface provided by the three NASA-funded Saildrones (SD1026, SD1060 and SD1061) (Hall et al., 2022; L'Hégaret et al., 2022) and the two NOAA-funded Saildrones (SD1063 and SD1064) (Quinn et al., 2021; L'Hégaret et al., 2022) deployed during the EUREC^{4}A-OA/ATOMIC campaigns. These uncrewed surface vehicles sampled the upper ocean and the air-sea interface (Zhang et al., 2019) at very high temporal and spatial resolution (SD1026, SD1060, SD1061 and SD1063 sample at 1-minute time resolution and SD1064 at 5-minute rate). The three NASA Saildrones along with SD1063 monitored the ocean eddy corridor near the South American coast (see Fig. 1 of Stevens et al. (2021) for specific locations) between January 17 and March 2, 2020, and January 13 and March 5, 2020, respectively. In turn, SD1064 passed over the eddy corridor and the open Atlantic Ocean (see Fig. 1 of Stevens et al. (2021) for specific locations) during the period of January 13 to April 11, 2020.

We use SST and SSS measurements from all five Saildrones during the entire sampling period (from January to April). These two variables are collected by a SeaBirdE37-SMP-ODO microcat at 0.5 m depth in all cases. To compute LHF, we also consider surface pressure, near-surface horizontal wind components, near-surface relative humidity, which we then convert to specific humidity, air temperature, and surface currents (only available in SD1063 and SD1064). Details on the various instruments that measure these variables and their installation heights are given in Table 1.

Table 1. Information on the devices measuring some of the air-sea interface variables used in this paper as well as their installed height in SD1063 and SD1064.

Variable	SD1063 device	SD1064 device	Installed
Air pressure	Vaisala Barometer 112790	Vaisala Barometer 1120788	0.2
RH / Air temperature	Rotronic HC2-S3 AT/RH	Rotronic AT/RH (0020245866)	2.3
Wind speed	Gill Anemometer (W182202)	Gill Anemometer (W181435)	5.2
Shortwave radiation	Delta-T Shaded Radiometer (A2047)	Delta-T Shaded Radiometer (A2045)	2.8
Longwave radiation	Eppley Radiometer (38873F3)	Eppley Radiometer (3277OF3)	0.8
Surface currents	Acoustic Doppler Current Profiler	Acoustic Doppler Current Profiler	-6

2.2 Satellite and Reanalysis Data

We rely on daily satellite maps of SST, SSS and Absolute Dynamic Topography (ADT) to provide a broad overview of the environmental conditions in which the *in-situ* measurements take place.

The salinity maps are from the SMAP-SSS Level 3, 8-day running mean gridded product (Meissner et al., 2019). This product provides daily fields with a spatial resolution of 0.25 °. The product is optimized for the Northwest Tropical Atlantic in February 2020 and is designed to provide the best possible representation of Amazon plume variability. The product, its uncertainties, and the comparison between TSG salinity and satellite SSS are detailed in Reverdin et al. (2021).

Daily SST maps are derived from the MUR-JPL dataset. This satellite product provides high-resolution SST values distributed over a global 0.01° × 0.01° grid. SST values from the version 4 Multiscale Ultrahigh Resolution (MUR) Level 4 analysis (Chin et al., 2017) are based on nighttime observations from several instruments, including the NASA Advanced Microwave Scanning Radiometer-EOS (AMSR-E), the JAXA Advanced Microwave Scanning Radiometer 2 on GCOM-W1, the Moderate Resolution Imaging Spectroradiometers (MODIS) on the NASA Aqua and Terra platforms, the US Navy WindSat microwave radiometer, the Advanced Very High Resolution Radiometer (AVHRR) on several NOAA satellites, and *in-situ* SST observations from the NOAA iQuam project. Daily results are obtained using a multi-scale variational approach that combines all available observations.

The satellite-based LHF is taken from the SeaFlux dataset (Clayson et al., 2014). The SeaFlux version used in this paper is called SeaFluxV3 and uses a nonlinear neural network technique to estimate near-surface air properties from microwave radiances (Roberts et al., 2010). To compute surface turbulent fluxes from near-surface variables, SeaFlux uses a neural network version of the COARE3.0 algorithm (Fairall et al., 2003). This dataset has a spatial resolution of nearly 25 km and a temporal resolution of 1 hour. Only daily averages of LHF are considered for the period 2008-2018.

To better understand the surface ocean circulation around the *in-situ* measurements, we use the daily ADT maps at 0.25 ° resolution from the AVISO product (Ducet et al., 2000). It combines data from all available satellites for the period 1993 to present. With this ADT field, the TOEddies algorithm developed by Laxenaire et al. (2018) identifies

eddies and their trajectories using the closed contours of the ADT as well as the maximum geostrophic velocity associated with the eddy. We also evaluate the seafloor depth map in the NWTA using the ETOPO2 dataset (Smith & Sandwell, 1997) at a 2-minute latitude/longitude spatial resolution.

To investigate the behavior of the marine atmospheric boundary layer height (MABLH) in regions where atmospheric *in-situ* data are missing, we use the ERA5 reanalysis (Hersbach et al., 2020). Note that ERA5 does not include coupling with an ocean model, but it is forced at the lower boundary by the Hadley Center Sea Ice and Sea Surface Temperature (HadISST) dataset as well as the Climate Change Initiative (ESA-CCI) until 2007 (Merchant et al., 2014) and the Operational Sea Surface Temperature and Ice Analysis (OSTIA) in the modern period (Donlon et al., 2007). ERA5 has a spatial resolution of $0.25° \times 0.25°$ and a time resolution of 1 hour. We consider only the MABLH between 2^{nd} and 5^{th} and between 16^{th} and 19^{th} of February 2020, which we collocate with the corresponding *in-situ* observations as described in section 1 of the Appendix.

3 Methodology

Prior to all calculations, we remove the diurnal cycle from several atmospheric and air-sea interface variables using a (multi-channel) singular spectrum analysis ((MC-)SSA) (Groth et al., 2017) as the imprint of diurnal warming on the near-surface circulation introduces an additional LHF variability source which masks the effects of some of the processes we want to assess here. The reader is referred to section 2 of the Appendix for a more detailed discussion on this point.

3.1 Water Mass Detection

We apply a *k-means* clustering method (Lloyd, 1982) to the SST-SSS fields from all five Saildrones to separate the different water masses sampled in the NWTA. We choose the Saildrone data fields to perform *k-means* because they sample the NWTA extensively (Fig. 2a): from the relatively quiet open ocean to the active NBC eddy corridor region near the South American coast. In addition, their sampling period is the longest among all other sampling devices: from 13^{th} January to 11^{th} April 2020.

k-means requires a predetermined number of k clusters, followed by a series of evaluations to assess the performance of the previous clustering. The k mutually exclusive clusters are characterized by its centroid, and the SST-SSS observations are grouped according to their distance to this centroid in SST-SSS space, with the condition that the sum of the squared Euclidean distance within each cluster is minimized. After several tests, we set $k = 6$. This choice identifies six water masses with different oceanic vertical structures and allows us to link them to the physical mechanisms and situations in which they were formed.

3.2 Ocean Vertical Structure

We study the vertical stratification of the ocean using all the temperature, salinity, and density profiles collected by the 4 RVs. First, we apply a linear interpolation to all the vertical profiles to fill missing values and filter them with a 5 point moving average (2.5 m) to eliminate small-scale noise. Then, we compute the mixed layer depth (MLD) from the vertical density profiles as in Y. Chen et al. (2022). To do so, we first estimate the gradient (first derivative) and curvature (second derivative) of the profiles using central differences. The derivatives along the profile edges are computed with one-sided differences. We then estimate the MLD as the depth with the maximum level of curvature, closest to the absolute maximum in potential density anomaly gradient, exceeding the surface density value by more than 0.03 kg m^{-3} and whose vertical gradient is greater than 0.0015 kg m^{-4}. Among other gradient and threshold methods, we find

this MLD detection algorithm to be very sensitive to the effects of salinity variations on density in the NWTA.

$$\text{MLD} = \text{depth where} \begin{cases} \frac{\partial^2 \sigma_0}{\partial z^2} \text{ maximum closest to the } \frac{\partial \sigma_0}{\partial z} \text{ absolute maximum} \\ \sigma_0 > \sigma_{0,surf} + 0.03 \\ \frac{\partial \sigma_0}{\partial z} > 0.0015 \text{ kg m}^{-4} \end{cases} \tag{1}$$

where σ_0 is potential density anomaly with respect to a reference pressure of 0 dbar. In regions with strong salinity-driven stratification, such as river plumes, there may be some decoupling between haline and thermal stratification. Therefore, to characterize the relative importance of salinity in ocean stratification, we rely on the OSS_{MLD} indicator (Maes & O'Kane, 2014; Gévaudan et al., 2021):

$$OSS_{MLD} = \frac{\langle N_S^2 \rangle}{\langle N^2 \rangle}, \tag{2}$$

where angle brackets denote vertical integrals in the ocean profile down to the MLD, namely

$$\langle \bullet \rangle_{\text{MLD}} = \frac{1}{\text{MLD}} \int_{-MLD}^{0} \bullet \quad dz \tag{3}$$

N^2 represents the Brunt-Väisälä frequency and accounts for the total stratification of the ocean. It is expressed in terms of the density profile, the Earth's gravity (g), and the reference seawater density (ρ_0), which we set here to 1026 g kg^{-3} as in Gévaudan et al. (2021):

$$N^2 = -\frac{g}{\rho_0} \frac{\partial \rho \left(T, S\right)}{\partial \text{z}} \tag{4}$$

The Brunt-Väisälä frequency can be decomposed as the sum of the stratification due to temperature (N_T^2) and the stratification due to salinity (N_S^2):

$$N^2 = N_S^2 + N_T^2, \tag{5}$$

with

$$N_S^2 = \frac{g}{\rho_0} \frac{\partial \rho \left(T_0, S\right)}{\partial \text{z}} \quad \text{and} \quad N_T^2 = \frac{g}{\rho_0} \frac{\partial \rho \left(T, S_0\right)}{\partial \text{z}}. \tag{6}$$

T_0 and S_0 are constant representative temperature and salinity values equal to the average temperature and salinity values in the ML of each vertical profile. Like in Hernandez et al. (2016), we choose to calculate N_S^2 as the difference between N^2 and N_T^2. Therefore, OSS_{MLD} is the contribution of the salinity stratification N_S^2 to the total stratification N^2, both averaged in the ML, expressed as a percentage of N^2.

The decoupling of haline and thermal stratification leads to the formation of barrier layers (BLs) (Godfrey & Lindstrom, 1989; Lukas & Lindstrom, 1991). A quick inspection of all temperature, salinity, and density profiles shows that a shallow layer of

constant salinity corresponding to the Amazon plume coexists with a thicker layer where temperature does not either decrease monotonically or remain almost constant. The former represents the actual ML computed from the density profiles while the latter corresponds to the existing ML before the inflow of the plume. As in de Boyer Montégut et al. (2004) and de Boyer Montégut et al. (2007), we define the lower boundary of that second layer (hereafter referred to as THERM) as the deepest level at which a temperature decrease of 0.2 °C occurs with respect to the 10 m-depth temperature:

$$\text{THERM} = \text{depth where}\,[T = T_{10m} - 0.2\ ^{\circ}C] \tag{7}$$

We choose the 10 m depth temperature as the reference to avoid the effects of diurnal warming (we do not remove the diurnal cycle from the ocean vertical profiles as justified in section 2 of the Appendix). Thus, the barrier layer thickness (BLT) is defined as the difference between THERM and MLD, where THERM is deeper than MLD (Sprintall & Tomczak, 1992). The presence of a BL limits the interaction between the ML and the ocean interior by inhibiting vertical water motion, thereby controlling the MLD heat content (OHC_{MLD}) per unit of area, which we estimate as:

$$OHC_{MLD} = \int_{MLD}^{0} \rho_0 C_p \left(T - T_{MLD}\right) \quad dz \tag{8}$$

where C_p is the specific heat capacity of seawater and T is water temperature. The presence of a surface fresh layer inhibits vertical mixing in the ocean as the layer's density is lower than that of the ocean below it. This situation is reversed if the surface fresher layer SST is lowered sufficiently by an amount ΔT that its effect on density (α ΔT) overcomes the stable density stratification provided by salinity (-β ΔS). Where ΔS is the salinity difference between the fresh ML and the salinity just below it, β is the salinity contraction coefficient, and α is the thermal expansion coefficient. The values used for all constants are given in the table 2. For a given cooling rate (Q), the temperature change achieved over an ocean layer of depth equal to the MLD in time Δt is:

$$\Delta T = \frac{Q\Delta t}{\rho_0 C_p MLD}. \tag{9}$$

Thus, the time taken to achieve the drop in temperature ΔT which overcomes ΔS reads (Mahadevan et al., 2016):

$$\Delta t = \frac{\rho_0\ C_p\ MLD}{Q} \frac{\beta\ \Delta S}{\alpha}. \tag{10}$$

Within the Amazon River plume, THERM is significantly deeper than the shallow MLD driven by salinity stratification. As shown in the next section, we often found warm temperature layers (and temperature inversions) trapped between the MLD and THERM, whose excess stored heat is not always released to the atmosphere. An estimate of this heat is given by the following expression:

$$\text{Heat potentially released} = \frac{OHC_{THERM} - OHC_{MLD}}{\Delta t}. \tag{11}$$

Note that this heat release is not necessarily in the form of LHF. An increase in SHF and surface outgoing long wave radiation (OLR) occur at the same time. We will return to this point later.

So far, all calculations have been based on the vertical temperature, salinity, and potential density anomaly profiles. However, we also estimate the MLD from the SD1063

ADCP current shear profiles where no collocated vertical temperature, salinity and density profiles are available. To do this, we first perform a linear interpolation to the current profiles to fill missing values. Then, we compute the vertical shear profiles by applying a central difference scheme to the zonal and meridional ocean current vertical profiles. We expect the well-mixed ML to have a uniform current velocity. Thus, to identify the MLD, we select the absolute shear maximum, and if it exceeds a threshold of $5\ 10^{-4}$ s^{-1} (an empirical value chosen by the authors which works well for the data used as it avoids spurious MLD values related to small-scale peaks), it is considered to be an estimate of the MLD.

Table 2. Characteristic values of the different seawater coefficients used in the analysis of the vertical ocean profiles. All of them are computed from temperature, salinity and pressure using the TEOS-10 Python module (Commission et al., 2015).

Constant	Value
ρ_0 [kg m^{-3}]	1026
C_p [J kg^{-1} K^{-1}]	3850
α [K^{-1}]	$3.5\ 10^{-4}$
β [kg g^{-1}]	0.78

3.3 Air-sea Interface

We compute LHF using the air-sea interface data from the RV *Atalante* meteorological mast, SD1063 and SD1064. This paper uses the COARE3.5 bulk algorithm to obtain LHF from SST, surface winds, surface humidity, and air temperature by applying the Monin-Obukhov Similarity Theory (MOST) (Fairall et al., 1996; Weller & Anderson, 1996; Fairall et al., 2003; Edson et al., 2013). No rainfall or wave related corrections are considered, and fluxes are calculated from bulk SSTs. In addition, the cool skin correction to the SST is included in the LHF calculation when TSG SST data are involved.

To quantify the contribution of each LHF forcing variable to the flux variation, we follow the methodology used in Tanimoto et al. (2003); Chuda et al. (2008); Yang et al. (2016). After some mathematical steps (see Appendix) it can be shown that:

$$\Delta LHF = \rho_a L_e C_e [\underbrace{\Delta U\,(\overline{q_s} - \overline{q})}_{\Delta \mathrm{LHF_U}} + \underbrace{\overline{U}\Delta q_s}_{\Delta \mathrm{LHF_{q_s}}} \underbrace{-\overline{U}\Delta q}_{\Delta \mathrm{LHF_q}} + \underbrace{\Delta U\,(\Delta q_s - \Delta q)}_{\Delta \mathrm{LHF_{U,\Delta q}}}] + \text{Residual.} \qquad (12)$$

Here, overbars denote time averages and Δs represent the deviations from those averages. $\Delta\mathrm{LHF}_U$ represents the contribution of anomalous wind speed, $\Delta\mathrm{LHF}_{q_s}$ the contribution of anomalous saturation specific humidity (in other words, SST), and $\Delta\mathrm{LHF}_q$ the contribution of anomalous specific humidity. $\Delta\mathrm{LHF}_{U,\Delta q}$ is the effect on LHF due to the covariance between the anomalous wind speed and the specific humidity deficit, defined as the difference between saturation specific humidity and specific humidity. Finally, the residual ensures that the LHF budget closes. ρ_a, L_e, and C_e represent air density, latent heat of evaporation, and moisture exchange coefficient, respectively. They are obtained with COARE3.5 and averaged over time. The error associated with this averaging is included in the residual.

However, this decomposition does not distinguish between the large-scale and small-scale (oceanic mesoscale and below) contributions to ΔLHF, as *in-situ* data contain the

influence of all the different spatial scales. We know from the literature that this distinction is particularly important in the wind speed response, which is directly influenced by small-scale SST anomalies and surface currents (Renault et al., 2019).

To isolate the small-scale SST anomalies from the large-scale signal, we first identify the SST-SSS front as the mean SST value when the sampling device crosses the boundary between a low-salinity and a high-salinity water mass. We then estimate the small-scale SST anomalies (SST') as the difference between each SST value in the time series and this reference temperature. We then convert the small-scale SST anomalies to wind speed anomalies by multiplying by the coupling coefficient in the first row of table 3 (α_{TFB}):

$$\Delta U_{TFB} = \alpha_{TFB}\ SST'. \tag{13}$$

The TFB contribution to the LHF is then computed by inserting $\Delta \mathrm{U}_{TFB}$ into the terms $\Delta \mathrm{LHF}_U$ and $\Delta \mathrm{LHF}_{U,\Delta q}$ of the equation 12. To evaluate the impact of the CFB, we recall how the coupling with surface flows is performed in models (Renault et al., 2019). In a one-dimensional flow, the wind speed value of the equation is 12:

$$U = U_a - U_o, \tag{14}$$

where U_a is the measured wind speed and U_o surface currents. In addition, surface currents feed back into U by an amount $\Delta \mathrm{U}_{CFB}$:

$$\Delta U_{CFB} = \alpha_{CFB}\ U_o \tag{15}$$

where α_{CFB} is the coupling coefficient between the surface current relative vorticity and the curl of surface winds. It is given in the second row of table 3. Therefore, to estimate the effect of the CFB on the LHF, we first compute the terms $\Delta \mathrm{LHF}_U$ and $\Delta \mathrm{LHF}_{U,\Delta q}$ from equation 12 using the wind velocity resulting from equation 14. Then we calculate the same two terms using the winds from the difference between equations 14 and 15. The difference between the two estimates of $\Delta \mathrm{LHF}_U$ + $\Delta \mathrm{LHF}_{U,\Delta q}$ corresponds to CFB effect.

Table 3. Information on the different coupling coefficients.

Coefficient	Description	Value	Reference
α_{TFB}	SST and near-surface wind magnitude	0.44 m s^{-1} °C^{-1}	Fernández et al. (2023)
α_{CFB}	surface current vorticity and near-surface wind curl	0.3 (unitless)	Renault et al. (2019)

3.4 Atmospheric Vertical Structure

Data from ARTHUS and the DLs are used to study the vertical structure of the atmosphere. Following Acquistapace et al. (2022), we apply some preprocessing to remove noise and analyze the atmospheric response to the SSS-SST gradients. First, we remove values outside reasonable ranges. The selected valid ranges for the different variables are: from 0 to 20 g kg^{-1} for WVMR, from 270 to 310 K for air temperature, from -5 to 5 m s^{-1} for vertical wind speed, and from 0 to 20 m s^{-1} for horizontal wind speed. Since the air temperature decreases with height, its valid range is only between 200 and

3000 m. Then we define the cloud base height (CBH) as 100 m (experimental value adopted by the authors) below the height where the largest vertical gradient in the BR occurs, as in Wang and Sassen (2001). The ARTHUS and DL values higher than the cloud base height are masked as they are known to be unreliable within the clouds (Lange et al., 2019).

We compute the marine atmospheric boundary layer height (MABLH) from the vertical LIDAR profiles after removing the diurnal cycle and applying the pre-processing described above. To this effect, we apply a rolling variance along each of the vertical WVMR profiles. We define the MABLH as the first maximum in the vertical WVMR variance profiles that exceeds a threshold of 0.2 g^2 kg^{-2} below 1200 m height (experimental value adopted by the authors).

To increase the robustness of our results, we also include the MABLH computed from the different RSs launched from the *Atalante* (Stephan et al., 2021). As in Acquistapace et al. (2022), we assign an SST and SSS value from the *Merian* TSG to each RS. Then, we compute the virtual potential temperature gradient ($\frac{d\theta_v}{dz}$) starting from a height level of 200 m. For a given height level, we calculate the mean and standard deviation of the distribution composed of all the vertical gradient values underneath. If the difference $\frac{d\theta_v}{dz}$ of the given height level and the mean of the distribution, as well as those from the three following levels exceed two times the standard deviation, then the MABLH is taken as the mean height between the above mentioned three vertical levels. This methodology has been found to disregard the high wind shear values close to the surface (likely due to the fast RS movements after the deployment) while accounting for the presence of several θ_v inversions. The reader is referred to section 3 of the Appendix for an intercomparison of different methods to compute MABLH from RS data.

Finally, we also compare the results with the collocated ERA5 MABLHs (more details on the collocation procedure in section 1 of the Appendix). Following Renault et al. (2019) and as described in Fernández et al. (2023), the mesoscale MABLH anomalies are isolated from the large-scale signal using a spatial filter. The MABLH field is smoothed with an isotropic Gaussian spatial filter with a standard deviation of 4 grid points at 0.25°. Gaussian weights that are located at a distance greater than 3 standard deviations of the Gaussian (σ) are assumed to be zero. The Gaussian filter is thus applied to a (6σ + 1)×(6σ + 1), which is 25 × 25 points, and is roughly equivalent to 6° × 6°. The filter cutoff is about 250 km. Small scale anomalies of the MABLH are defined as MABLH' = MABLH - [MABLH], where [MABLH] is the smoothed field.

4 Results

4.1 A Very Heterogeneous Region: Water Mass Identification

The spatial distribution of the 6 surface water masses identified by the 5 Saildrones with *k-means* is shown in Fig. 2a and their position in the T-S diagram in Fig. 2b. North of Barbados, the domain is mostly dominated by the North Atlantic Subtropical Waters (NASWs) (similar to the NASWs in Olivier et al. (2022)) in light green (SSS < 35.9 psu). The clustering analysis also detects waters with the same SST-SSS centroid at 9 °N, 52.5 °W, shown in dark green. These waters are saltier than the NASWs (SSS > 35.9 psu). For simplicity, we include both waters in the same water mass, the green cluster waters (GCWs), since they all have SSTs around 26.72 °C. In the transect from 13.5 °N to 8 °N, the farthest from the coast, we find the saltiest and coldest waters of the region (the cluster centroid values are 36.1 psu and 26.3 °C, in blue). Again, in Fig. 2 we distinguish between the waters with SSS less than 35.9 psu (dark blue), located north of 13 °N, and those with SSS > 35.9 psu (cyan), to highlight the different origins and locations. However, we will refer to these waters as cyan cluster waters (CCWs). They are also found in coastal upwelling systems, as shown later.

Closer to the coast, from 8°N to Barbados, we find four different water masses. In indigo we show the retro-reflection waters (RWs), which are warm and salty (SST-SSS centroid of 27.22 °C-36.16 psu). They are located south of 9 °N and east of Trinidad and Tobago and are trapped within an anticyclonic NBC ring (A2 of Olivier et al. (2022)). North of the NBC retroflection we find the modified retroflection waters (MRWs) in purple. They are slightly warmer than the RWs (SST centroid of 27.37 °C) and much fresher as a consequence of their interaction with the Amazon River outflow (SSS centroid of 35.56 psu).

Finally, we detect two low salinity clusters represented in gold and salmon colors Fig. 2. The golden waters are the warmest and freshest (SST-SSS centroid of 28.17 °C-30.6 psu) and are associated with the Amazon River plume. We refer to them hereafter as Amazon plume waters (APWs). They are found in the south of the NWTA, close to the continental shelf and mostly in the spring when the Amazon River discharge is at its highest during the period of study. The salmon cluster is also very fresh (33.87 psu as SSS centroid), but colder than the golden cluster (27.09 °C as SST centroid). It results from the mixing of the colder and saltier RW and MRWs with the APWs, which are enhanced by the local ocean surface circulation induced by the NBC rings. In this paper, we call them modified Amazon plume waters (MAPWs).

The vertical ocean structure of the 6 water masses is shown in Fig. 3. The GCWs and CCWs have uniform vertical profiles of temperature, salinity, and density down to the MLD, which is about 20 m (Fig. 3a, and b). The location of THERM is not significantly different from that of the MLD in the case of CCW whereas it is much deeper for GCW as a consequence of the presence of temperature inversions.

RWs and MRWs (Fig. 3c and d respectively) show a well mixed salinity (between 35 and 36 psu) and density profile accompanied by a 45 to 55 m thick layer of almost constant temperature. Below this layer the temperature decreases. In both cases, the MLD lies below the THERM. In fact, over RWs we find the thickest MLDs of all the region (more than 100 m thick).

Salinity profiles of the APWs and MAPWs (Figs. 3e and f, respectively), on the other hand, show a 10 m thick low-salinity layer associated with the Amazon plume, the base of which delimits the MLD. Temperature and density are also constant in this layer. Below the MLD, however, salinity and density decrease sharply while temperature remains constant until 20 m depth. It is the imprint of the ML prior to the advent of the plume. This situation creates a BL of about 10 m depth in APWs. Regarding MAPWs, THERM is located below the 2 °C temperature inversion at 80 m depth. In both cases, there is also a slight salinity change at the same depth as the temperature inversion.

We also look at the evolution of LHF, 5.2 m wind speed (U_{5m}), 2.3 m specific humidity (q_{2m}), 2.3 m air temperature (T_{2m}), and SST over the different clusters as a function of SSS (Fig. 4). Fig. 4a shows reduced fluxes (around 150 W m^{-2}) for APWs and up to 34 psu and then a jump of 50 W m^{-2}. LHF is on average higher from 34.5 psu, but with a large spread. Furthermore, U_{5m} (Fig. 4b) oscillates between 6 and 10 m s^{-1} with slightly lower values over the low salinity water masses. The SSS binning of q_{2m}, T_{2m} and SST is shown in Figs. 4c, d and e respectively. It shows larger values for the three variables over the low SSSs (19 g kg^{-1} for q_{2m}, 27.5 °C for T_{2m}, and 28.2 °C for SST) and smaller values over saltier waters (16.5 g kg^{-1}, 26.8 °C, and 27.1 °C). The trends in these three variables contribute to the increase of LHF at high salinity and are in agreement with the satellite climatologies of the NWTA, which show that higher (lower) specific humidity near (far) the coast and lower (higher) winds contribute to the decrease (increase) of LHF in this part of the region (open ocean) as shown in Fernández et al. (2023) and Fig. 1b. However, Fig. 4 does not allow us to separate the contributions of the different forcing variables to the overall change in LHF. In the following sections, we aim to understand the different mechanisms leading to changes in the forcing variables

and LHF, distinguishing between ocean, atmosphere, and air-sea interface processes, as well as between spatial scales. We do this with three study cases where the devices mentioned in section 2.1 cross the freshwater Amazon plume.

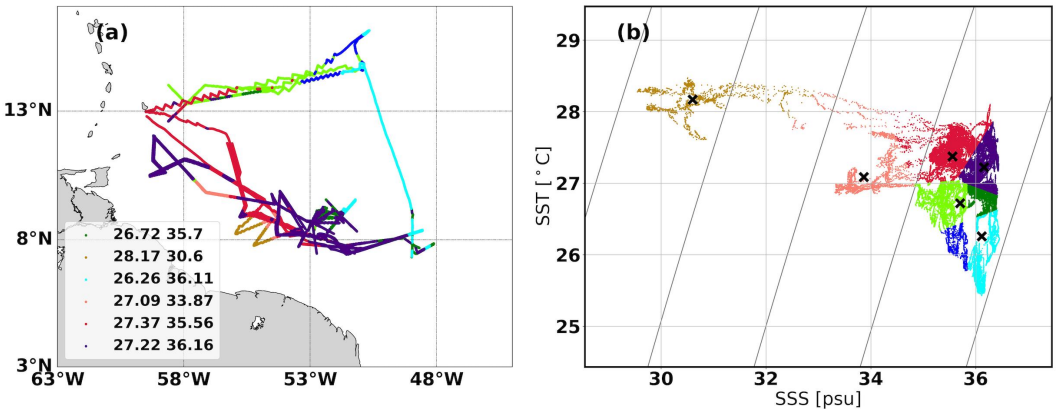

Figure 2. (a) Saildrone tracks color-coded by SST-SSS clusters. The values of the cluster centroids are shown in the legend, where the first value corresponds to the SST (in °C) and the second value represents the SSS (in psu). (b) T-S plot of all SST-SSS measurements taken by the Saildrones, color-coded with the water masses. The black crosses indicate the position of each cluster centroid in the diagram. Note that the green and cyan clusters are split in two according to an SSS threshold of 35.9 psu to account for the different origins of the water subtypes.

4.2 Case 1: RVs *Atalante* and *Merian* Sample SSS-SST Front Caused by the Interaction between the Amazon Plume and a Cold Coastal SST Patch

Between the 2^{nd} and the 5^{th} of February 2020, RVs *Atalante* and *Merian* sampled a cold SST patch several times, as shown in Fig. 5a. It developed near the coast of Suriname, probably as a consequence of an upwelling event (Acquistapace et al., 2022). The negative SST anomaly is associated with a cyclonic eddy in the ADT field, which we name C1 (Fig. 5b). TOEddies also detects the presence of the NBC ring (A1) at 7 °N and 51 °W. The combined circulation of the two rings advects warm (Fig. 5a) and fresh waters (Fig. 5b) to the northwest, creating a 2 °C-6 psu SST-SSS gradient. As a result, four different water masses were sampled: APW and MAPW towards the interior of the ocean and GCW and CCW closer to the continental shelf (Fig. 5a).

Fig. 6a contains the along track SST (red) and SSS (blue) values from the *Atalante* TSG. It shows that the SSS remained above 34 psu for the first 400 km and then dropped as the MAPWs and APWs were sampled. At the same time the SSTs crossed the 27 °C threshold. We select four representative locations along the track (crosses in Fig. 6a) and examine their vertical ocean structure. In Fig. 6b we observe a 30 m thick well-mixed temperature and salinity ML, with THERM 10 m above its base. As this profile belongs to the MAPWs, the SST is greater than 27 °C and the OSS_{MLD} index is greater than 50 %, meaning that salinity dominates over temperature in driving the stratification. However, as we approach the boundaries of the plume, but still in the MAPWs (in the transition between GCWs and MAPWs, Fig. 6c), we find that salinity and temperature contribute equally to the stratification (OSS_{MLD} = 49 %) and that the MLD is shallower than THERM (10 m and 25 m, respectively). In between, we observe a warm subsurface layer with a temperature anomaly of 0.7 °C warmer than the ML at its peak. In turn, the SST does not reach 27 °C. On the other hand, the CCW profile (Fig. 6d) shows

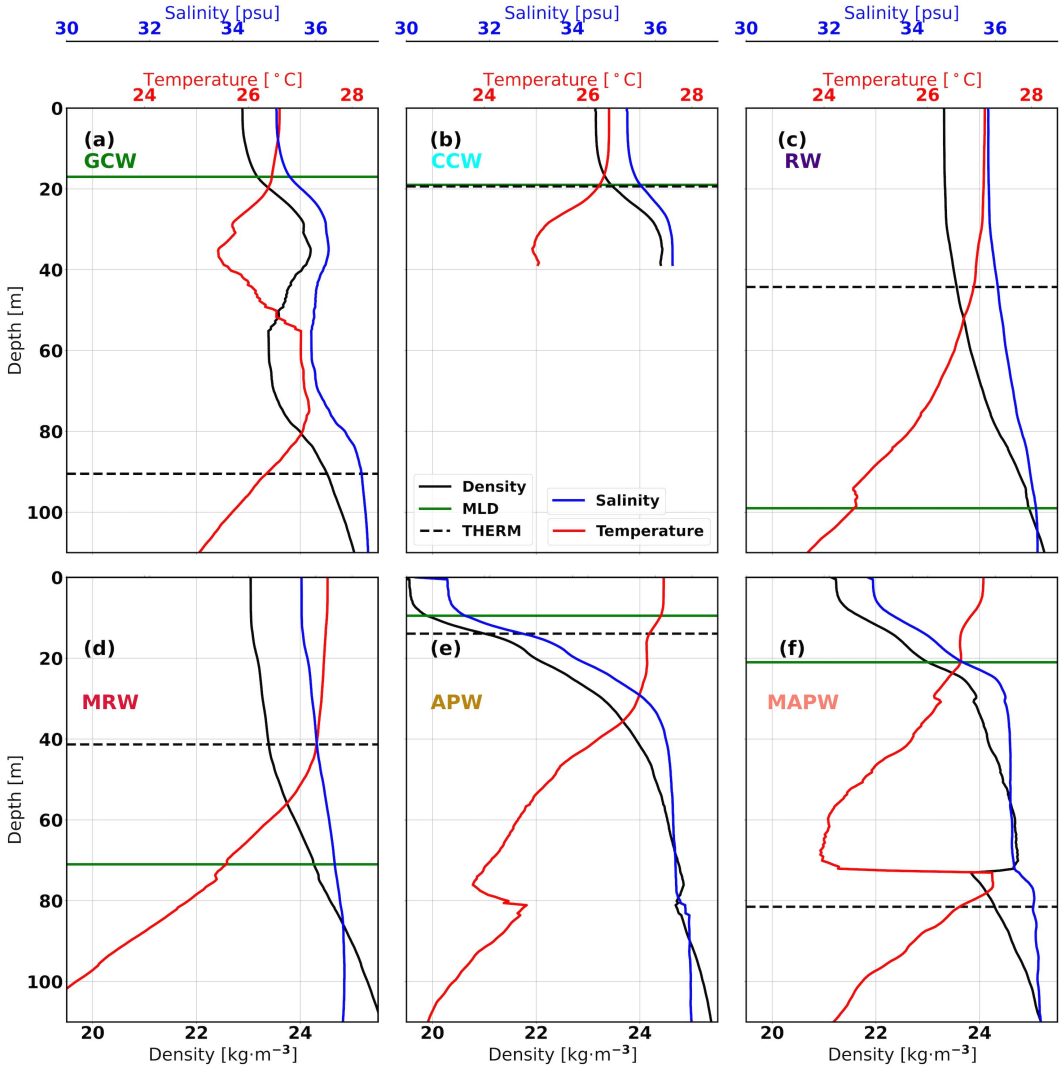

Figure 3. Mean vertical profiles of temperature (red), salinity (blue), and density (black) for (a) GCWs, (b) CCWs, (c) RWs, (d) MRWs, (e) APWs, and (f) MAPWs. In all figures, the solid green line marks the MLD and the dashed black line marks THERM. Data are collected from all ocean vertical profile sampling devices in the section 2.1 between January 17 and February 16, 2020.

a well mixed 20 m thick ML. Here MLD and THERM lie very close to each other and the BL is not able to develop as much as the other clusters. In addition, seawater temperature dominates over salinity in driving stratification (OSS_{MLD} of 45 %). Finally, the APW profile (Fig. 6e) shows a strong decoupling between thermal and haline stratification with a very fresh and warm ML of less than 10 m (OSS_{MLD} = 72 %, salinity controlled stratification). THERM lies deeper than 30 m. Between the MLD and THERM we observe a layer of constant temperature with decreasing salinity (as shown in Fig. 3f) which represents the existing ML before the inflow of the Amazon plume.

MLD estimates from all track locations derived from the *Atalante* MVP density profiles show the same tendency (Fig. 7a, plotted as a function of RV *Atalante* TSG SSS, and color-coded with the TSG SST). Shallow 10 m MLs are observed up to 32 psu, and their values increase with increasing SSS (decreasing SST), with MLDs as deep as 50 m.

The OSS_{MLD} index shows the opposite tendency (Fig. 7b). For low salinity values (APW and MAPW), salinity controls the vertical stratification of the ocean and the OSS_{MLD} index shows values as high as 80% - 90%. Once the SSS exceeds the value of 34 psu, the OSS_{MLD} index starts to decrease and for the saltiest (coldest) part of the front, its values are less than 50%, meaning that the vertical stratification is controlled by sea temperature.

To quantify the decoupling between the influence of temperature and salinity on stratification, we compute the BLT as the difference between THERM and MLD when the former is deeper than the latter (Fig. 7c). The BLTs are thicker within the APW (up to 30 m, in agreement with Fig. 6e) and between SSS values of 34 to 35 psu (about 10 to 20 m), in agreement with Fig. 6c and d respectively. The OHC difference between THERM and the MLD computed with eq. 8 shows the same pattern (Fig. 7d), as it is proportional to the BLT by construction. However, it is interesting to focus on the increase of the OHC difference between 34 and 35 psu, which is accompanied by higher SSTs (light blue and some orange colors in the scatter dots). It corresponds to the heat stored in the subsurface warm layers found at the boundaries of the Amazon plume (Fig. 6c, transition between MAPWs and GCWs). When the MLD salinity becomes large enough, the MLD waters become negatively buoyant and the atmospheric forcing (winds and radiative cooling of the boreal winter) is strong enough to overcome the plume-driven stratification, so that the subsurface warm layers are brought to the surface, increasing the SST and hence LHF. Therefore, we calculate the amount of heat potentially released using eq. 11 between 34 and 35 psu (Fig. 7e) and obtain values between 0 and 35 W m^{-2}, being the median of the distribution 1.8 W m^{-2}. Note that this heat might not only be transferred to the atmosphere in the form of LHF, we also observe an increase in SHF and outgoing longwave radiation (OLR) as a result of the SST variations. However, they are small compared to the LHF change. Using COARE3.5 and the Stefan-Boltzmann law with the wind, humidity, temperature, and SST values shown in Fig. 4, a 0.4 °C SST increase as observed between Fig. 6b and c leads to an LHF increase of 15.9 W m^{-2}, a SHF increase of 3.3 W m^{-2}, and an OLR increase of 2.5 W m^{-2}. However, for simplicity, we consider the histogram in Fig. 7e to represent LHF only.

LHF is also influenced by the overlying atmospheric conditions and the atmospheric response to SST and surface currents. Previous research has already discussed the fast atmospheric response to this cold SST patch and its associated SSS gradient (Acquistapace et al., 2022), but failed to distinguish between spatial scales (mesoscale and below as opposed to large scales) and to evaluate its impact on LHF. Here we aim to answer the last two questions. To do so, we collocate the ARTHUS/DL vertical profiles measured by the RV *Merian* with the *Merian* TSG as described in section 1 of the Appendix, and select the warmest 25% and the coldest 25%. A more detailed analysis of the horizontal wind speed and specific humidity vertical profiles follows in section 4 of the Appendix. Figs. 8a and b show that the warmest (coldest) profiles in salmon (cyan) are characterized by higher (lower) horizontal and vertical wind speeds at all levels. In turn, the warmest profiles down to 600 m have higher specific humidity than the coldest, in contrast to the situation above 600 m where the coldest profiles are more humid (Fig. 8c). Whereas vertical velocity profiles seem to be in agreement with DMM, horizontal wind velocity vertical profiles do not. According to DMM we would expect higher surface wind speed over warm waters as observed, but also a larger wind shear owing to the decoupling between the MABL and the free troposphere. This last feature is not observed as horizontal wind speeds are lower in the coldest profiles for all the height levels. Thus, it seems that the changes in the horizontal wind speed profiles are more linked to temporal variations rather than spatial variations as discussed in Acquistapace et al. (2022). Indeed, the warmest profiles are all located at the end of the TSG SST time series. We come back to this point in the following paragraphs.

To check the MABLH thickness variations, Fig. 8d contains the box plots of the coldest (left) and warmest (right) MABLH distributions using ARTHUS (red), the 60 *Atalante* RS (blue), and ERA5 (light green). In all three cases the MABLH is higher over the warm side with values ranging from 750 to 1250 m. This result is consistent with the DMM mechanism and previous studies using bulk models of trade wind MABL dynamics (Neggers et al., 2006; Zheng, 2019), which show a decrease in MABLH over colder waters. Although the three estimates show the same trend, there is a large spread and mismatch between them because they were measured by different instruments at slightly different locations and using different methodologies. However, not all of the variations in MABL thickness, wind speed, and humidity are explained by the DMM mechanism. It is true that the MABLH' (in green) becomes positive over the warmest ERA5 grid points (between 0 and 150 m, as opposed to the -50 - 100 m range over the coldest grid points), as expected from the DMM. However, the smoothed MABLH field ([MABLH], in olive green) also increases from the cold to the warm side, implying that the large-scale atmospheric conditions are partly responsible for the regime change in the atmosphere.

To evaluate the impact of the above mechanisms on LHF, we apply eq. 12 to the RV *Atalante* mast air-sea interface data. We include the coupling with surface currents in the wind speed using eq. 14 and the collocated ocean surface velocity derived from the X-band radar on the RV *Merian*. A comparison between eq 12 and a first-order numerical Taylor deconvolution can be found in section 5 of the Appendix. Fig. 9a shows the LHF deviations with respect to the along-track LHF mean between the 2^{nd} and the 5^{th} of February. It shows a large LHF difference between both sides of the front of $\sim$160 W m^{-2}, close to the climatological LHF value (Fig. 1b); the LHF is significantly lower over the cold SST patch. The near-surface wind influence (ΔLHF_U) shown in Fig. 9b is the main controlling factor of the LHF variation $\sim$100 W m^{-2}. As shown in Fig. 8a, APWs and MAPWs are associated with higher near-surface wind speeds and thus positive values of ΔLHF_U, which decrease as we move toward GCWs and CCWs.

The second most important term driving ΔLHF is ΔLHF_{q_s}, which represents LHF variations associated with SST changes and is shown in Fig. 9c. APWs and MAPWs are associated with larger SSTs and thus positive ΔLHF_{q_s} values between 10 W m^{-2} and 30 W m^{-2}. In turn, GCWs and CCWs are associated with negative ΔLHF_{q_s} values $\sim$-10 to -20 W m^{-2}. In the boundaries of the Amazon plume, we observe a ΔLHF_{q_s} increase of $\sim$5 W m^{-2} on average (black triangles), associated with the release of heat from the subsurface warm layer, which coincides with the mean value of the probability density function shown in Fig. 7e. Finally, the contributions of specific humidity (ΔLHF_q), the covariance between wind speed anomalies and specific humidity deficit anomalies ($\Delta\text{LHF}_{U,\Delta q}$) and the residual are second order contributions (Fig. 9d, e and f respectively). The first one shows values between -30 and 30 W m^{-2} over GCW and CCW with no clear tendency and the last two oscillate between 10 and -10 W m^{-2} over the whole SSS range.

Finally, we examine the total effect of wind speed on LHF (ΔLHF_U + $\Delta\text{LHF}_{U,\Delta q}$), separating the effects of the TFB, the CFB, and the large-scale atmospheric circulation. Their mean values over each cluster, color-coded with the water mass, are shown in the first, second, third, and fourth bars of each quartet in Fig. 10. Over the warm water masses (APW and MAPW), the near-surface wind speed increase associated with the DMM mechanisms causes a positive TFB effect on LHF (4.5 W m^{-2} and 2 W m^{-2}, respectively). Over the colder and saltier water masses (GCW and CCW), TFB has a negative effect on the LHF by reducing the near-surface winds. On the other hand, CFB always has a positive effect on LHF (except over APW where we lack collocated surface current data). This is due to the fact that trades flow towards the southwest while surface currents flow over most of the places towards the northeast (contours Fig. 5b, see local circulation induced by C1). To sum up, TFB and CFB significantly contribute to total wind contribution to LHF (ΔLHF_U + $\Delta\text{LHF}_{U,\Delta q}$) and can even drive the sign of it like in MAPWs.

4.3 Case 2: SD1063 Crossing a Weaker Amazon Plume Close to the NBC Retroflection

The NOAA-funded SD1063 crossed the northern edge of the Amazon plume between 16^{th} and 19^{th} in February 2020 (Fig. 11). The local ocean surface circulation is driven by two different structures: the warm anticyclonic ring A1 and the anticyclonic-cyclonic eddy pair A2-C2. The clockwise rotation of the surface waters around A1 advects cool waters coming from the same coastal cold patch of section 4.2 towards the northwest (Fig. 11a), which mix with the low-salinity Amazon plume waters (Fig. 11b). Thus, in this study case we work with two clusters: the cooler and fresher MAPWs in salmon and the warmer and saltier RWs in indigo (Fig. 11a).

Fig. 12 shows the binned distributions of different air-sea variables in both water masses. Note that, contrary to what happened in section 4.2, the fresh side of the front is cooler than the warm side of the front, although the SST difference is not as large: on average 0.4 °C as shown in Fig. 12a (as opposed to 2 °C). The specific humidity deficit, defined as the difference between the saturation specific humidity (q_s) and the specific humidity, also shows larger values over the RWs ($\sim$6 g kg^{-1}) than over the MAPWs ($\sim$4 g kg^{-1}), due to the SST changes via q_s and the background conditions that affect specific humidity as discussed later.

Fig. 12c shows that surface wind speeds were on average higher over RWs (mean values between 9 m s^{-1} and 10 m s^{-1}) than over MAPWs (mean values between 8 m s^{-1} and 9 m s^{-1}). The surface winds also experienced a shift in direction, from northeast in RWs ($\sim$-115 °) to east over MAPWs ($\sim$-100 ° to -90°), as shown in Fig. 12d, although there is a lot of overlap between the two PDFs. This is the expected distribution for a region where the trades dominate the near-surface atmospheric circulation. On the other hand, the velocity of the surface currents, shown in Fig. 12e, oscillates between 0.1 and 0.6 m s^{-1} in both cases, with average values slightly higher over the MAPWs due to the proximity of A2 and the associated compression of the ADT isolines (Fig. 11b). These surface currents have mean directions of about -45 ° for RWs and -55 ° with respect to the north for MAPWs, as shown in Fig. 12f. These directions are consistent with the ADT isolines of Fig. 11b, from which we can deduce a southwest-northeast motion as a consequence of the combined effect of the clockwise rotation of A1 and the counterclockwise rotation of C2.

To get an insight into the vertical structure of the ocean in both water masses, we use the SD1063 ADCP data to compute the MLD from the shear maximum (MLD_{shear}), since no collocated vertical profiles of ocean temperature, salinity, and density are available. The results are shown in Fig. 12g. Over MAPWs, the MLD is between 10 m and 50 m depth, while RWs shows MLD_{shear} values between 40 and 70 m, as we expect the low salinity Amazon plume intrusion to determine stratification and reduce the thickness of the ML. The ERA5 collocated MABLH (black triangles in Fig. 12) is shown as the solid line distribution in Fig. 12h. It shows larger MABLH values over RWs (between 800 and 1400 m) than over MAPWs (between 700 and 1200 m). However, the MABLH' representing small-scale MABLH variations (dashed distributions) covers the same range of values for both water masses. Considering the ERA5 MABLH as a reliable data source (see sections 1 and 4 of the Appendix for a detailed discussion), we conclude that the higher wind speed and lower specific humidity leading to an increase in the specific humidity deficit shown in Figs. 12b and c may not be fully related to a near-surface response to mesoscale SST anomalies via the DMM mechanism, but mainly to a change in background conditions.

To compute the LHF and analyze its spatial variations, we use COARE3.5 and the decomposition in eq. 12. The results are shown in Figs. 13a and b. LHF is on average 90 W m^{-2} higher over RWs than over MAPWs, mainly due to the large differences in specific humidity (green bars, ΔLHF_q, $\sim$60 W m^{-2} greater over RWs than over MAPWs)

as a first order contributor and wind speed variations (blue bars, $\Delta\mathrm{LHF}_U$, ∼15 W m^{-2} greater over RWs than over MAPWs). The LHF variation directly driven by SST (red bars, $\Delta\mathrm{LHF}_{q_s}$, ∼10 W m^{-2} greater over RWs than over MAPWs) is the third most important contribution in both cases (red bars), while the covariance between wind speed and specific humidity gradient ($\Delta\mathrm{LHF}_{U,\Delta q}$) and the residual, plotted in pink and orange, respectively, are the least important contributions.

These results suggest that the spatial flux variations (i.e. the differences between the gray bars in Fig. 13a and b) are mainly driven by the atmosphere. In the case of the wind speed related LHF variations ($\Delta\mathrm{LHF}_U$ + $\Delta\mathrm{LHF}_{U,\Delta q}$), we separate the influences of the background flow, the TFB and the CFB in Fig. 13c and d. They show that $\Delta\mathrm{LHF}_U$ + $\Delta\mathrm{LHF}_{U,\Delta q}$ is mainly driven by the background flow (green bar, ∼-7.5 W m^{-2} over MAPW versus ∼10 W m^{-2} over RWs), with the CFB playing a secondary role in MAPWs and RWs(∼-2 W m^{-2} and ∼2.5 W m^{-2} respectively). The TFB does not contribute significantly to $\Delta\mathrm{LHF}_U$ + $\Delta\mathrm{LHF}_{U,\Delta q}$ with less than 1 W m^{-2} variation in both cases.

We also assess the effect of heat release from the subsurface warm layer with the time series of SSS and $\Delta\mathrm{LHF}_{q_s}$, plotted in blue and yellow in Fig. 13e. They are displayed as a function of the distance to the SSS front defined between the last MAPW and the first RW measurements. The $\Delta\mathrm{LHF}_{q_s}$ and SST are not uniform on both sides of the front, especially over MAPWs. At a distance between 50 km and 10 km from the front in the MAPW domain, we find SSS values ranging from 34 psu to 35 psu (the boundaries of the Amazon plume, shown as vertical dashed lines) and a sharp increase in $\Delta\mathrm{LHF}_{q_s}$ (of ∼14 W m^{-2}), which then remains constant for the rest of the track. This $\Delta\mathrm{LHF}_{q_s}$ variation is of the same order of magnitude as the one shown in Fig. 7e, occurs in the same salinity range as the secondary $\Delta\mathrm{LHF}_{q_s}$ maximum in Fig. 9c and is analyzed over the same waters of section 4.2 which have onlyn been advected northwestward. These facts suggest that the jump in $\Delta\mathrm{LHF}_{q_s}$ could be related to heat release from the subsurface warm layer, although a more complete understanding of the vertical structure of the ocean and its evolution would be needed to verify this hypothesis. Finally, we also plot the alongshore MLD_{shear}. Consistent with Fig. 12g, it is shallower over MAPWs and deepens with increasing SSS in RWs.

4.4 Case 3: SD1064 Zigzagging across a Strong Amazon River Plume in Boreal Spring

Between 31st March and 11th April, SD1064 zigzagged across a very warm and fresh water tongue as shown in Figs. 14a and b. The freshwater plume detached from the Guiana Plateau at 6°N and was being steered northward by the induced circulation of the NBC ring A2 and the cyclonic C2 eddy (Fig. 14) as well as by NBC retroflection. It then began to expand northeastward toward the open ocean. Between March 31 and April 3, SD1064 sampled RWs and MRWs (in indigo and crimson, respectively, in Fig. 14a) and then entered and zigzagged across the plume, sampling APWs (in gold, the cluster with the lowest SSS centroid, 30.6 psu). This configuration gives an SST difference of less than 1 °C between the inside and outside of the plume, but a very large SSS difference of more than 6 psu.

Based on the SD1064 TSG measurements, SSS values remained constant during the first three days of RW and MRW sampling (∼36 psu) and then dropped to nearly 30 psu during the 5th of April (blue curve in Fig. 15a). On April 6, SD1064 exited the plume and the SSS increased abruptly to 36 psu, then dropped back to 30-31 psu as SD1064 re-entered the plume. SST measurements show the opposite pattern, remaining below 28 °C over RWs and MRWs and crossing the threshold during sampling of APWs. Note that the 28°C threshold is important because it provides moisture to the air column and favors tropical cyclone formation and intensification (Balaguru et al., 2012).

The total LHF anomaly time series, computed with respect to the mean LHF of the time period of this study case, is shown as a black line in Fig. 15b, and its variability is a consequence of the combined effects of ΔLHF_U and ΔLHF_q (blue and red lines in Fig. 15b, respectively). Between the 31^{st} of March and the 2^{nd} of April, SD1064 passed through a drier air mass (verified with the ERA5 specific humidity field, but not shown here), which increased ΔLHF_q and also Δ LHF, even though the wind speed anomalies and thus ΔLHF_U were negative during the same period. In fact, it is in the 2^{nd} of April that ΔLHF reaches its lowest value, $\sim$65 W m^{-2}. During the rest of the study period, ΔLHF variations were controlled by ΔLHF_U, which remained positive throughout most of the APW, in part due to the DMM mechanism. The fact that ΔLHF_U varies rapidly within hours and that ΔLHF_q shows less hourly variability reinforces the hypothesis that the specific moisture-associated flux changes originate from large-scale atmospheric variability.

Some of the second-order contributions to the LHF variations (ΔLHF_{q_s} in black, $\Delta\text{LHF}_{U,\Delta q}$ in blue, and the residual in red) are plotted in Fig. 15c. Except for the first three days, $\Delta\text{LHF}_{U,\Delta q}$ and the residual are negligible for most of the period. In turn, the direct influence of the SST on the flux (ΔLHF_{q_s}) induces an LHF difference of $\sim$45 W m^{-2} between the lowest point reached on the 2^{nd} of April over the MAPWs ($\sim$-25 W m^{-2}) and the highest point on the 9^{th} of April ($\sim$20 W m^{-2}). Finally, the TFB and CFB time series are shown in Fig. 15d. Except for the first three days of the time series, where there are significant negative TFB effects on the flux (between -10 W m^{-2} and -5 W m^{-2}), in the rest of the time series the TFB and CFB are negligible and of the same order as $\Delta\text{LHF}_{U,\Delta q}$ and the residual. Note that we do not plot the collocated ERA5 MABLH values in this study case: they are noisy and do not allow us to draw any conclusions. This fact highlights the limitations of ERA5 to properly characterize MABLH dynamics and the importance of ocean-atmosphere coupling, especially at the ocean small scales.

5 Discussion and Conclusions

The EUREC^{4}A-OA/ATOMIC field experiment provides a large set of air-sea interface measurements and collocated ocean and atmosphere vertical profiles to study the air-sea heat flux variability in the NWTA during the boreal winter and spring. Six distinct surface water masses are identified in the region. North of Barbados, the dominant water masses are the GCW and CCW with relatively cold temperatures and high salinities (Fig. 2a). These waters are the coldest and saltiest of all. We also detect them close to the continental shelf as a consequence of coastal upwelling or vertical mixing events (Acquistapace et al., 2022; Olivier et al., 2022). Still close to the South American coast, we find four different water masses with higher SSTs and a more heterogeneous SSS configuration. RW and MRW are shown in indigo and crimson, respectively. They are characterized by high temperatures and salinities ranging from 35 to 36 psu. Finally, the presence of the Amazon freshwater plume, which propagates into the open ocean, defines the APW and MAPW clusters. They are shown in gold and salmon, respectively.

Based on measurements of vertical ocean temperature and salinity profiles from gliders, MVPs, CTDs, and UCTDs, we observe that the upper ocean layers coinciding with APW and MAPW have a very different vertical structure than the other four water masses. In particular, they are characterized by a fast temperature decrease starting above 40 m depth and subsurface warm layers developing between 70 - 80 m depth, while the MLDs are considerably shallower (Fig. 3e and f). In contrast, RWs and MRWs show well mixed vertical profiles with 50 m thick layers of constant density, temperature and salinity (Fig. 3c and d). Air-sea interface *in-situ* data also show important differences between water masses (Fig. 4). For water masses characterized by salinities below 34 psu, the LHF is systematically lower (Fig. 4a). Our results suggest that this is mostly a consequence of increased specific humidity (Fig. 4c). ERA5 specific humidity snapshots show that over APWs, which will not be sampled by SD1064 until late March-April 2020, horizontal advection

of moist air from the southeast increases specific humidity. However, other local effects of the air-sea interaction may also be involved. Since ERA5 has limited resolution and does not reproduce the coupled ocean-atmosphere processes with complete realism, it is not possible to analyze them from the ERA5 outputs. In the present study, we focus on three different situations where the MAPWs and APWs intersect to understand the different mechanisms leading to such LHF variations over the different water masses.

The first case consists of the RVs *Atalante* and *Merian* crossing at different locations, but in a very short period of time, a cold and salty patch near the coast of Suriname, surrounded by the warm and fresh APWs and MAPWs. This creates a 2 °C SST and a 6 psu SSS gradient (Fig. 5). The RV *Atalante* MVP vertical profiles (Figs. 6b, c, d and e) show that the increase of SSS in the border of the plume (transition from MPWs to GCWs) favors the mixing of subsurface warm layers with the rest of the ML thereby increasing SST and leading to an additional heat release of up to 40 W m^{-2} locally as seen in Fig. 7e. Furthermore, the LHF decomposition indicates that SST and wind speed are the two leading factors influencing the change in LHF ($\Delta\text{LHF}_U \sim$ 100 W m^{-2} and $\Delta\text{LHF}_{q_s} \sim$ 40 W m^{-2} respectively out of a total of $\Delta\text{LHF} \sim$ 160 W m^{-2}) as shown in Fig. 9. Within the total wind speed influence ($\Delta\text{LHF}_U + \Delta\text{LHF}_{U,\Delta q}$), the changes in near-surface winds induced by mesoscale (and smaller scale) SST structures (TFB) and near-surface currents (CFB) are on average 10-30% depending on the water mass (Fig. 10). This result is in agreement with previous research using satellite observations and reanalysis (Fernández et al., 2023).

To substantiate these initial case study results, we examine two different time windows during which APWs and MAPWs are sampled by SD1063 and SD1064. The first occurred between 16^{th} and 19^{th} February 2020, when a weaker (more saline) freshwater plume was transported by the coastal current and the various NBC rings in the region up to 11°N (Fig. 11). Although the SST-SSS gradient is much weaker than in the first case (0.4°C - 2.5 psu), we are able to recover the influence of the same mechanisms. Excluding the effect of wetter conditions over the MAPWs (ΔLHF_q), wind speed is the leading variable for LHF changes, followed by SST (Fig. 13a and b) in agreement with the first case study. Within the total wind speed effect ($\Delta\text{LHF}_U + \Delta\text{LHF}_{U,\Delta q}$), background wind conditions dominate over both water masses, although the CFB significantly modulates $\Delta\text{LHF}_U + \Delta\text{LHF}_{U,\Delta q}$ in the MAPWs (Fig. 13c and d). Furthermore, we observe a sharp increase of ΔLHF_{q_s} ($\sim$14 W m^{-2}) between 34 and 35 psu as shown in Fig. 13e. We hypothesize that this variation comes from the subsurface warm layer heat release, as it is observed in the same salinity range than the first study case and the increase is compatible with Fig. 7e. Again, the buoyancy change due to the SSS increase in the borders of the plume enhances vertical motion and mixes the subsurface warm layers with the rest of the ML. As a consequence, surface waters become warmer and LHF_{q_s} increases locally. However, we lack data to evaluate this process in more detail, and it remains a research question for modeling studies. Finally, the third study case consists of SD1064 crossing a warm and prominent Amazonian plume between March 31^{st} and April 11^{th} 2020 (Fig. 14). The relative importance of the different decomposition terms in the total change of the LHF is consistent with the second case.

The processes described here highlight the complexity of the interactions that drive LHF changes even in boreal winter (and spring), when the atmospheric state in the Northwest Tropical Atlantic is relatively stable and the Amazon plume is weak. To verify that the mechanisms assessed here are still present and contribute to the overall flux change in the same way, more *in-situ* measurements in other seasons, such as boreal summer and/or other years, would be highly recommended. They would also be useful for a better understanding of the interannual variability of the LHF. Furthermore, the influence of the diurnal cycle (which was removed from the beginning) in all the results presented here remains an open research question to be addressed in a future dedicated paper.

This study is limited by the scarcity of data in the region and highlights the importance of collocated ocean, atmosphere, and air-sea interface observations to accurately quantify the various factors influencing heat fluxes and the MABL. As the Amazon plume has only been sampled in three different cases with different background conditions and seasons, more observations of ocean and atmosphere vertical profiles further south, closer to the minimum SSS values of the Amazon River plume, would help us to better quantify its influence on the LHF and heat fluxes in general. In addition, it would be valuable to check how all the mechanisms described above are reproduced in fully coupled regional ocean-atmosphere models and/or high-resolution regional atmospheric models forced with different SST products. In particular, different simulations with different Amazon River plume intensities would be very useful. Even if these simulations are not able to reproduce all the processes included in the observations, they would allow a statistical approach to the problem instead of a case study approach, thus providing more robust estimates of the contribution of each controlling variable to the change in the LHF.

Appendix: Further Information on Methodology

1 Intercomparison between ERA5 and *in-situ* SST and Collocation Procedure

Throughout the manuscript, the ERA5 output is collocated with various *in-situ* observations like Saildrones or TSGs. Following Hall et al. (2022), we use the closest-neighbor interpolation technique, to match the locations and times of the corresponding *in-situ* product with the nearest location and time available in the ERA5 products. Because of the spatial and time resolutions of ERA5 (0.25 ° and 1 hour respectively), only collocations within this resolution are included. To be consistent with Hall et al. (2022), the closest points in space are collocated before the closest points in time.

However, this operation introduces some inaccuracies in the atmospheric response as ERA5 does not include coupling with the ocean and its resolution is too coarse to detect some of the small-scale ocean features whose impacts we are interested in to assess (Hersbach et al., 2020). Hence, this subsection aims to show how well ERA5 SST and the TSG SST from the study cases 1 and 2 match. The reasons to use SST and not other variable is because mesoscale SST is the ultimate driver of MABLH' changes.

The metrics used to compare ERA5 to *in-situ* observations are the standard deviation of the difference (STD), the mean difference and the Spearman correlation coefficient. The resulting time series from the collocation are shown in Fig. 16 and the statistics in table 4. We observe from Fig. 16a that ERA5 seems to reproduce fairly well the SST values and variability (Spearman correlation coefficient of 0.86) being the *Merian* TSG SST 0.17 °C warmer on average. This result, together with the fact that the RSs from the *Atalante* were incorporated in the production of the ERA5 output encourages us to rely on the ERA5 MABLH values plotted in Fig. 8d. On the contrary, during the study case 2, ERA5 is not able to capture neither the SST variability nor its values being the Spearman coefficient close to zero. Nevertheless, the MABLH values shown in Fig. 12d seem to reproduce the expected behavior with thicker MABLs in the warm side of the front. To elucidate the exact causes of this result would require a closer examination on the ERA5 MABLH parametrization and remains beyond the scope of this study. What is clear is that ERA5 might not always correctly reproduce MABLH changes as the forcing itself does not coincide with the observations. However, due to the lack of MABLH observations, we include ERA5 output in our results.

2 Diurnal Cycle Removal

This section provides a deeper insight into the methodology employed to remove the diurnal cycle in this manuscript: the (multichannel) singular spectrum analysis (MC-

Table 4. Mean difference and standard deviation (STD) for ERA5 minus the corresponding *in-situ* observations as well as the Spearman correlation coefficient and its p-value for Case 1 and Case 2. The number of samples in both cases is included in the last row.

Metric	**Case 1**	**Case 2**
Mean (°C)	-0.17	0.09
STD (°C)	0.15	0.19
Spearman Correlation	0.86	-0.01
p-value	0.00	0.69
Number of samples	389	4753

SSA) (Ghil et al., 2002; Groth et al., 2017). It is a natural method of extracting oscillatory modes of variability from a (multivariate) time series. Here, we detail the steps followed for SSA, although the process can be generalized for several variables as in Groth et al. (2017). Let us consider a variable's time series (SST, near-surface wind, air temperature...) from which we remove the mean and divide by the standard deviation ($\tilde{X}$(t)):

$$\tilde{X}(t) = \{X(t), X(t+1), ...X(N)\}\,. \tag{1}$$

We aim to compute the *lag-covariance* matrix (C) as in Vautard and Ghil (1989) and Ghil et al. (2002). In order to do that we first define the *embedded time series* matrix (Y). The general formulation for an element of Y in the i-th row and the j-th column reads:

$$y_{i,j} = X(i+j-1). \tag{2}$$

Following the definition of covariance of a time series with zero mean and unit variance we define C as follows:

$$C = \frac{Y'\,Y}{N} \tag{3}$$

If we define M as the *window size*, only the first N-M+1 rows of C will be filled with non-zero values. In this manuscript, we choose M to be equal to 4 days as a compromise value. It cannot be too large because then we would be mixing information in the diurnal cycle reconstruction from very different water masses but it cannot be smaller than 1 day either. The choice of N as a normalization factor in eq. 3 is motivated by the fact that N>>M for all the cases in this study. We then diagonalize C to obtain its eigenvectors (ρ_k) and its eigenvalues (λ_k) such that:

$$C\rho_k = \lambda_k \rho_k. \tag{4}$$

Projecting the matrix Y onto each eigenvector (ρ_k) yields the corresponding principal component (PC_k):

$$PC_k = Y\rho_k. \tag{5}$$

These PCs are orthogonal at lag zero, which means that there is no covariance between different PCs. In addition, the variance represented by each PC_k is given by the corresponding eigenvalue λ_k. Finally, one can perform a reconstruction of the variable time series based on a group of PCs (K) such that:

$$RC_{\mathrm{K}}(t) = \frac{1}{M_t} \sum_{k\in \mathrm{K}} \sum_{j=L_t}^{U_t} PC_k(t-j+1)\rho_k(t). \tag{6}$$

Being the normalization factor (M_t) and the lower and upper bound of summation (L_t and U_t respectively) (Ghil & Vautard, 1991; Vautard et al., 1992):

$$(M_t, L_t, U_t) = \begin{cases} \left(\frac{1}{t}, 1, t\right) & \text{for} \quad 1 \leq t \leq M-1 \\ \left(\frac{1}{M}, 1, M\right) & \text{for} \quad M \leq t \leq N-M+1 \\ \left(\frac{1}{N-t+1}, t-N+M, M\right) & \text{for} \quad N-M+2 \leq t \leq N \end{cases} \tag{7}$$

Therefore, to remove the diurnal cycle we compute the different PCs of a given time series with eq. 5. We compute their power spectrum and select the ones (usually a couple) whose dominant period is one day (allowing a tolerance of ± 1 h) and whose cumulative explained variance is less than 70%. This is a value taken by the authors to ensure that the PCs representing the diurnal cycle contain an important part of the variance. Hence, we reconstruct the diurnal cycle using eq. 6 with the selected PCs and the time series without the diurnal cycle with the rest of the PCs.

One of the advantages of removing the diurnal cycle this way instead of using an averaged diurnal cycle is that it allows us to recover a space-time varying diurnal cycle as shown in Fig. 17a. We observe that the SST diurnal's cycle amplitude is larger over the APWs and the MAPWs (golden) than in the rest of the water masses (crimson). As the mixed layer depth gets shallower, it can be heated or cooled more easily. The effects of this space-time varying diurnal cycle on air-sea interface heat fluxes will be further studied in a future dedicated paper.

Finally, we need to assess the issue whether the diurnal cycles we obtain contain more variance than we would expect if they were generated by noise. Since the PCs are mutually orthogonal, our null-hypothesis is that the data have been generated by an autoregressive process of order 1: AR(1) (Allen & Smith, 1996). This choice is also motivated by the fact that AR(1) processes are incapable of supporting the oscillatory behavior we are interested in detecting. Having formulated the null-hypothesis, we generate a large ensemble of surrogate data segments (5000 realisations of the noise model consisting in a generic AR(1) process) with the same length as $\tilde{X}(\mathrm{t})$. We compute the variance associated to the PCs of each realisation as before. The resulting 5% and 95% percentiles of the variance distribution from the surrogate data segments are represented as errorbars in Fig. 17b and the variances associated to the PCs derived from $\tilde{X}(\mathrm{t})$ are the red squares. We observe that there is a pair of PCs at a 1 day period which lie above their surrogate data bars corresponding to a statistically significant diurnal cycle.

In order to know the variables from which we need to remove the diurnal cycle, we perform the significance test to each variable's time series and assess if the daily peaks lie above the surrogate distribution or not. Table. 5 provides a the list of the variables and devices from which the diurnal cycle is removed. For ARTHUS and DLs, we apply the MC-SSA, which is a generalization of SSA for variables with more than one dimension (in this case time and height). Finally, the diurnal cycle is not removed from the ocean vertical profiles because data are not equally spaced in time. It constitutes one of the shortcomings of this study.

3 MABLH Computation from RSs

Here, we compare three different methods to compute the MABLH from the RSs as there is no universal technique to treat RS data. Before calculating the MABLH, we first perform a linear interpolation to all vertical profiles to fill missing values. Then, we smooth air temperature, winds and surface water vapor mixing ratio using a 5 point running average (equivalent to 50 m in height) like in Hande et al. (2012) or Peng et al. (2023). We perform this operation in order to remove small-scale features in the vertical pro-

Table 5. List of variables and devices from which the diurnal cycle is removed and methodology based upon the AR(1) test. Surface pressure from Saildrones and the RV *Atalante* mast had a very prominent semi-diurnal peak which was also removed.

Variable(s)	Instrument(s)	Methodology
SST, RH_{2m}, u_{5m}, v_{5m}, T_{2m}	Saildrones (NASA + NOAA)	SSA
SST, RH_{2m}, u_{5m}, v_{5m}, T_{2m}	RV *Atalante* mast	SSA
u, v, w, WVMR	ARTHUS and DLs	MC-SSA

files which might result in spurious MABLH values. We also disregard in all the calculations the first 200 m of the atmosphere to avoid the influence of the surface layer and the fast and erratic movements of the RS after the deployment.

First, we use the Richardson bulk number (Ri_B) method proposed by (Vogelezang & Holtslag, 1996). Ri_B is defined, for a given height, as the ratio between the turbulence associated with the vertical temperature gradient and the turbulence generated by wind shear. In this paper we ignore the effects of surface friction in the calculation of Ri_B. Thus, according to (Seidel et al., 2012) we have:

$$Ri_B = \frac{\left[\frac{g}{\theta_{vs}}\right]\left[\theta_{vz} - \theta_{vs}\right]\left[z - z_s\right]}{\left(u_z - u_z\right)^2 + \left(v_z - v_z\right)^2}, \tag{8}$$

where θ_v is the virtual potential temperature and u and v are the zonal and meridional wind components. The subscripts "s" denote the values of the variables at a reference level (z_s) that we choose to be closest to the surface. Thus, the MABLH is the lowest level at which Ri_B exceeds 0.25, as in Davison et al. (2013) and Seidel et al. (2012).

Second, we try the virtual potential temperature gradient ($\frac{d\theta_v}{dz}$) method (or parcel method) from Hande et al. (2012). We estimate it using central differences and the derivatives along the edges are computed with one-sided differences. Then, the MABLH is estimated as the absolute maximum of the gradient between 200 m and 1200 m. We impose a lower limit in the gradient in order to ensure that the main inversion is greater than 0.01 $K{\cdot}m^{-1}$. This is the case in 99 % of the profiles.

Finally, we consider a slight modification of the virtual potential temperature gradient method. To ensure the potential temperature inversion at the top of the MABL is maintained in height, we first obtain the height level where the difference between the local $\frac{d\theta_v}{dz}$ and the mean of all the $\frac{d\theta_v}{dz}$ below exceeds two standard deviations from the distribution formed by all the $\frac{d\theta_v}{dz}$ below the given level height. If this condition is matched in three consecutive height levels we consider the MABLH to be the mean of the above mentioned three height levels.

Fig. 18 shows the vertical structure of the atmosphere at different locations in the time period of case 1 (each one in a row). The first location (Figs. 18a, b and c) shows that when there is a well-mixed MABL with constant θ_v and then a decrease at the top of the MABL, the parcel method and the modified parcel method give similar MABLH values (Fig. 18b). On the contrary, the Ri_B method shown in Fig. 18c shows an unrealistically low MABLH value of little more than 200 m. In fact, the Ri_B method is very affected by the high wind shear values usually found close to the surface (Figs. 18a) even if the θ_v vertical profile remains homogeneous. This fact might also explain the MABLH values around 200 m for the cold side of the front observed by Acquistapace et al. (2022).

Given that θ_v is mostly constant up to 1 km, we discard the Ri_B method to compute the MABLH.

In the second location (Figs. 18d, e and f), we observe that the parcel method yields a MABLH of 850 m (Fig. 18e) which coincides with the Ri_B value (Fig. 18f) associated with a peak in the wind shear at that same height (Fig. 18d). However, from the θ_v vertical profile we can observed that the well-mixed MABLH reaches 600 m, as indicated by the black line representing the modified parcel algorithm value. In fact, the parcel method fails to provide a correct value of the MABLH when there are several inversions in the θ_v profile.

Even when there is a single inversion the parcel method can slightly overestimate the MABLH as we observe in the third location (Figs. 18g, h and i). Fig. 18h shows a MABLH slightly over the start of the θ_v inversion. In this case the Ri_B method also overestimates the MABLH Fig. 18i. Thus, we choose the modified parcel method to estimate the MABLH from RSs.

4 Extended Analysis of the Atmospheric Vertical Profiles from RSs and ERA5

In Figs. 8a, b and c we display the mean vertical profiles of horizontal wind speed, vertical wind speed and specific humidity from ARTHUS and the DLs to assess the atmospheric response in the first case study. We include in this section the mean vertical profiles of horizontal wind speed and specific humidity from the RSs and collocated ERA5 (Fig. 19).

The wind speed atmospheric response from the *Atalante* RSs (Fig. 19a) resembles to the one from the DLs. Weaker wind speeds dominate over the cold side of the front (cyan). However, there is a large spread and overlapping between profiles, probably as a consequence of the reduced number of observations (#15 here as opposed to #96 for the DLs). This larger spread is linked to the broad RS MABLH PDFs in Fig. 8d as well. The specific humidity vertical profiles are displayed in Fig. 19b, and show that drier conditions predominate over the cold side of the front. The overlapping between the warmest and coldest profile is once again very important.

The ERA5 horizontal wind response opposes to those from the observations (RSs and DL/ARTHUS) as displayed in Fig. 19c. Higher wind speeds are observed over the cold side of the front and reduced winds dominate over the warm side with little overlapping between vertical profiles. In turn, the specific humidity vertical profiles in Fig. 19d show that a drier MABL is expected over the warm side of the front in agreement with the ARTHUS humidity profiles (Fig. 8c).

To conclude, ERA5 and observations (RSs and DL/ARTHUS) present a different wind speed vertical structure even though if ERA5 SST seems to correctly reproduce the observation SST values and variability(Fig. 16a). We hypothesize that the possible misrepresentation of MABL air-sea interaction processes in ERA5 might lead to unsatisfactory atmospheric vertical structures, especially regarding horizontal wind speed. This fact limits the reliability of the ERA5 MABLH results we present in the main text.

5 Numerical and Analytical LHF Decompositions

Following Tanimoto et al. (2003); Chuda et al. (2008); Yang et al. (2016) we apply a Reynolds decomposition to near-surface wind speed, saturation specific humidity and specific humidity which we generically denote as X

$$X = \overline{X} + \Delta X, \tag{9}$$

where $\overline{X}$ is the time-mean averaged over the time period of each study case and ΔX the anomaly with respect to that mean from each value of the time series. We then consider the bulk formula for LHF from COARE3.5:

$$LHF = \rho_a \; L_e \; C_e \; U \;\; (q_s - q)\,, \tag{10}$$

where ρ_a is air density, L_e the latent heat of evaporation and C_e the moisture exchange coefficient. Considering these three parameters as constants and applying eq. 9 to the rest of the variables in eq. 10 we obtain:

$$LHF = \rho_a \; L_e \; C_e \left[\overline{U}\,\overline{q_s} + \Delta U\overline{q_s} + \overline{U}\Delta q_s + \Delta U \Delta q_s - \overline{U}\,\overline{q} - \Delta U\overline{q} - \overline{U}\Delta q - \Delta U \Delta q\right] \tag{11}$$

Averaging eq. 11 we get:

$$\overline{LHF} = \rho_a \; L_e \; C_e \;\; \left[\overline{U}\,(\overline{q_s} - \overline{q}) + \cancelto{0}{\overline{\Delta U\,(\Delta q_s - \Delta q)}}\right] = \rho_a \; L \; C_e \left[\overline{U}\,\overline{q_s} - \overline{U}\,\overline{q}\right] \tag{12}$$

Therefore

$$\Delta LHF = LHF - \overline{LHF} = \rho_a \; L_e \; C_e \left[\Delta U\overline{q_s} + \overline{U}\Delta q_s + \Delta U \Delta q_s - \Delta U\overline{q} - \overline{U}\Delta q - \Delta U \Delta q\right] \tag{13}$$

which is eq. 12 except for the residual to ensure the LHF budget closes. We also tested the numerical first-order Taylor-series deconvolution approach as in Kwiatkowski and Orr (2018) to check if we could reduce the residual. In this case, a given LHF anomaly (ΔLHF) is expressed as:

$$\Delta LHF = \underbrace{\left(\frac{\partial LHF}{\partial U}\right)\Delta U}_{\Delta \mathrm{LHF_{wspd}}} + \underbrace{\left(\frac{\partial LHF}{\partial q}\right)\Delta q}_{\Delta \mathrm{LHF_{qair}}} + \underbrace{\left(\frac{\partial LHF}{\partial T}\right)\Delta T}_{\Delta \mathrm{LHF_{tair}}} + \underbrace{\left(\frac{\partial LHF}{\partial SST}\right)\Delta SST}_{\Delta \mathrm{LHF_{SST}}} + \mathrm{Residual}, \tag{14}$$

where the partial differentials are estimated numerically as the slope of the regression between LHF and the corresponding variable setting the other variables constant their mean values of the study case time period. ΔU, Δq, ΔT and ΔSST are changes in input variables (wind speed, specific humidity, air temperature and sea-surface temperature respectively), synchronous with ΔLHF. They are also computed with respect to the study case time period mean. Residual is a term necessary to close the LHF budget resulting from numerical errors when performing the partial derivatives.

The results from the numerical Taylor deconvolution are shown in Fig. 20. When comparing with Fig. 9, we observe that the wind speed and specific humidity contributions (Figs. 9b and 20d; Figs. 9d and 20c) are very similar. In addition, the changes in SST are represented via the q_s in the analytical decomposition (Fig. 9c) which resembles to the pattern of Fig. 20e. The residuals of the two decompositions (Figs 9f and Fig. 20f) have the same order of magnitude, being the the one from the Taylor decomposition (Fig. 20f) slightly smaller. Perhaps, it is a consequence of the fact that the error associated to the averaging of C_e, L and ρ_a (which depend on air temperature) is separated into $\Delta \mathrm{LHF}_T$ (Fig. 20d) and not isolated in the numerical decomposition.

Even if the residual is slightly smaller in the first-order Taylor numerical decomposition, we use the analytical method throughout the main text so that we avoid making numerical errors. Besides, it enables us to interpret the different terms of the LHF budget in an easier and straightforward manner.

Appendix A Availability Statement

We benefited from numerous data sets made freely available and listed here:

- All the *in-situ* measurements taken from the 4 RVs and the autonomous vehicles (Saildrones, ARGO or gliders): `https://observations.ipsl.fr/aeris/eurec4a/#/`
- SeaFlux, `https://seaflux.org/seaflux$\_$data/ATOMIC$\_$current/`
- ERA5, `https://cds.climate.copernicus.eu/cdsapp#!/dataset/reanalysis-era5-single-levels?tab=form`
- MUR-JPL, `https://thredds.jpl.nasa.gov/thredds/ncss/grid/OceanTemperature/MUR-JPL-L4-GLOB-v4.1.nc/dataset.html`
- SMAP maps produced by Remote Sensing System (RSS v4 40 km) `https://doi.org/10.5285/5920a2c77e3c45339477acd31ce62c3c`
- Altimetry product produced by Ssalto/Duacts and distributed by CMEMS `https://data.marine.copernicus.eu/products`.
- ETOPO2 seafloor depth `https://sos.noaa.gov/catalog/datasets/etopo2-topography-and-bathymetry-natural-colors/`

Acknowledgments

The authors gratefully acknowledge the contributions from Drs. Meghan Cronin and Samantha Wills from NOAA for the fruitful discussions. We also warmly thank the captain and crew of RVs *Atalante*, *Merian*, *Meteor* and *Ronald H. Brown*.

References

Acquistapace, C., Meroni, A. N., Labbri, G., Lange, D., Späth, F., Abbas, S., & Bellenger, H. (2022). Fast atmospheric response to a cold oceanic mesoscale patch in the north-western tropical atlantic. *Journal of Geophysical Research: Atmospheres*, *127*(21), e2022JD036799.

Allen, M. R., & Smith, L. A. (1996). Monte carlo ssa: Detecting irregular oscillations in the presence of colored noise. *Journal of climate*, *9*(12), 3373–3404.

Anderson, S. P., Weller, R. A., & Lukas, R. B. (1996). Surface buoyancy forcing and the mixed layer of the western pacific warm pool: Observations and 1d model results. *Journal of Climate*, *9*(12), 3056–3085.

Andrade-Canto, F., & Beron-Vera, F. (2022). Do eddies connect the tropical atlantic ocean and the gulf of mexico? *Geophysical research letters*, *49*(20), e2022GL099637.

Balaguru, K., Chang, P., Saravanan, R., Leung, L. R., Xu, Z., Li, M., & Hsieh, J.-S. (2012). Ocean barrier layers' effect on tropical cyclone intensification. *Proceedings of the National Academy of Sciences*, *109*(36), 14343–14347.

Bishop, S. P., Small, R. J., Bryan, F. O., & Tomas, R. A. (2017). Scale dependence of midlatitude air–sea interaction. *Journal of Climate*, *30*(20), 8207–8221.

Breugem, W.-P., Chang, P., Jang, C., Mignot, J., & Hazeleger, W. (2008). Barrier layers and tropical atlantic sst biases in coupled gcms. *Tellus A: Dynamic Meteorology and Oceanography*, *60*(5), 885–897.

Buck, A. L. (1981). New equations for computing vapor pressure and enhancement factor. *Journal of Applied Meteorology and Climatology*, *20*(12), 1527–1532.

Bye, J. A. (1985). Large-scale momentum exchange in the coupled atmosphere-ocean. In *Elsevier oceanography series* (Vol. 40, pp. 51–61). Elsevier.

Chelton, D. B., Esbensen, S. K., Schlax, M. G., Thum, N., Freilich, M. H., Wentz, F. J., ... Schopf, P. S. (2001). Observations of coupling between surface wind stress and sea surface temperature in the eastern tropical pacific. *Journal of Climate*, *14*(7), 1479–1498.

Chen, L., Jia, Y., & Liu, Q. (2017). Oceanic eddy-driven atmospheric secondary circulation in the winter kuroshio extension region. *Journal of Oceanography*, *73*, 295–307.

Chen, Y., Speich, S., & Laxenaire, R. (2022). Formation and transport of the south atlantic subtropical mode water in eddy-permitting observations. *Journal of Geophysical Research: Oceans*, *127*(1), e2021JC017767.

Chin, T. M., Vazquez-Cuervo, J., & Armstrong, E. M. (2017). A multi-scale high-resolution analysis of global sea surface temperature. *Remote sensing of environment*, *200*, 154–169.

Chuda, T., Niino, H., Yoneyama, K., Katsumata, M., Ushiyama, T., & Tsukamoto, O. (2008). A statistical analysis of surface turbulent heat flux enhancements due to precipitating clouds observed in the tropical western pacific. *Journal of the Meteorological Society of Japan. Ser. II*, *86*(3), 439–457.

Clayson, C. A., Roberts, J. B., & Bogdanoff, A. (2014). Seaflux version 1: a new satellitebased ocean-atmosphere turbulent flux dataset. *Int J Climatol (submitted)*.

Commission, I. O., et al. (2015). The international thermodynamic equation of seawater–2010: calculation and use of thermodynamic properties.[includes corrections up to 31st october 2015].

Dai, A., & Trenberth, K. E. (2002). Estimates of freshwater discharge from continents: Latitudinal and seasonal variations. *Journal of hydrometeorology*, *3*(6), 660–687.

Davison, J. L., Rauber, R. M., Di Girolamo, L., & LeMone, M. A. (2013). A revised conceptual model of the tropical marine boundary layer. part i: Statistical characterization of the variability inherent in the wintertime trade wind regime over the western tropical atlantic. *Journal of the atmospheric sciences*, *70*(10), 3005–3024.

de Boyer Montégut, C., Madec, G., Fischer, A. S., Lazar, A., & Iudicone, D. (2004). Mixed layer depth over the global ocean: An examination of profile data and a profile-based climatology. *Journal of Geophysical Research: Oceans*, *109*(C12).

de Boyer Montégut, C., Mignot, J., Lazar, A., & Cravatte, S. (2007). Control of salinity on the mixed layer depth in the world ocean: 1. general description. *Journal of Geophysical Research: Oceans*, *112*(C6).

Didden, N., & Schott, F. (1993). Eddies in the north brazil current retroflection region observed by geosat altimetry. *Journal of Geophysical Research: Oceans*, *98*(C11), 20121–20131.

Donlon, C., Robinson, I., Casey, K., Vazquez-Cuervo, J., Armstrong, E., Arino, O., ... others (2007). The global ocean data assimilation experiment high-resolution sea surface temperature pilot project. *Bulletin of the American Meteorological Society*, *88*(8), 1197–1214.

Ducet, N., Le Traon, P.-Y., & Reverdin, G. (2000). Global high-resolution mapping of ocean circulation from topex/poseidon and ers-1 and-2. *Journal of Geophysical Research: Oceans*, *105*(C8), 19477–19498.

Edson, J. B., Jampana, V., Weller, R. A., Bigorre, S. P., Plueddemann, A. J., Fairall, C. W., ... Hersbach, H. (2013). On the exchange of momentum over the open ocean. *Journal of Physical Oceanography*, *43*(8), 1589–1610.

Fairall, C. W., Bradley, E. F., Hare, J., Grachev, A. A., & Edson, J. B. (2003). Bulk parameterization of air–sea fluxes: Updates and verification for the coare algorithm. *Journal of climate*, *16*(4), 571–591.

Fairall, C. W., Bradley, E. F., Rogers, D. P., Edson, J. B., & Young, G. S. (1996). Bulk parameterization of air-sea fluxes for tropical ocean-global atmosphere coupled-ocean atmosphere response experiment. *Journal of Geophysical Research: Oceans*, *101*(C2), 3747–3764.

Fernández, P., Speich, S., Borgnino, M., Meroni, A. N., Desbiolles, F., & Claudia, P. (2023). On the importance of the atmospheric coupling to the small-scale ocean in the modulation of latent heat flux. *Frontiers in Marine Science*, *10:1136558*.

Foltz, G. R., & McPhaden, M. J. (2009). Impact of barrier layer thickness on sst in the central tropical north atlantic. *Journal of Climate*, *22*(2), 285–299.

Fournier, S., Chapron, B., Salisbury, J., Vandemark, D., & Reul, N. (2015). Comparison of spaceborne measurements of sea surface salinity and colored detrital matter in the amazon plume. *Journal of Geophysical Research: Oceans*, *120*(5), 3177–3192.

Fratantoni, D. M., & Glickson, D. A. (2002). North brazil current ring generation and evolution observed with seawifs. *Journal of Physical Oceanography*, *32*(3), 1058–1074.

Fratantoni, D. M., & Richardson, P. L. (2006). The evolution and demise of north brazil current rings. *Journal of Physical Oceanography*, *36*(7), 1241–1264.

Frenger, I., Gruber, N., Knutti, R., & Münnich, M. (2013). Imprint of southern ocean eddies on winds, clouds and rainfall. *Nature geoscience*, *6*(8), 608–612.

Garraffo, Z. D., Johns, W. E., Chassignet, E. P., & Goni, G. J. (2003). North brazil current rings and transport of southern waters in a high resolution numerical simulation of the north atlantic. In *Elsevier oceanography series* (Vol. 68, pp. 375–409). Elsevier.

Gaube, P., Chickadel, C., Branch, R., & Jessup, A. (2019). Satellite observations of sst-induced wind speed perturbation at the oceanic submesoscale. *Geophysical Research Letters*, *46*(5), 2690–2695.

Gévaudan, M., Jouanno, J., Durand, F., Morvan, G., Renault, L., & Samson, G. (2021). Influence of ocean salinity stratification on the tropical atlantic ocean surface. *Climate Dynamics*, *57*(1-2), 321–340.

Ghil, M., Allen, M., Dettinger, M., Ide, K., Kondrashov, D., Mann, M., ... others (2002). Advanced spectral methods for climatic time series. *Reviews of geophysics*, *40*(1), 3–1.

Ghil, M., & Vautard, R. (1991). Interdecadal oscillations and the warming trend in global temperature time series. *Nature*, *350*(6316), 324–327.

Godfrey, J., & Lindstrom, E. (1989). The heat budget of the equatorial western pacific surface mixed layer. *Journal of Geophysical Research: Oceans*, *94*(C6), 8007–8017.

Groth, A., Feliks, Y., Kondrashov, D., & Ghil, M. (2017). Interannual variability in the north atlantic ocean's temperature field and its association with the wind stress forcing. *Journal of Climate*, *30*(7), 2655–2678.

Hall, K., Daley, A., Whitehall, S., Sandiford, S., & Gentemann, C. L. (2022). Validating salinity from smap and hycom data with saildrone data during eurec4a-oa/atomic. *Remote Sensing*, *14*(14), 3375.

Hande, L., Siems, S. T., Manton, M. J., & Belusic, D. (2012). Observations of wind shear over the southern ocean. *Journal of Geophysical Research: Atmospheres*, *117*(D12).

Hayes, S., McPhaden, M., & Wallace, J. (1989). The influence of sea-surface temperature on surface wind in the eastern equatorial pacific: Weekly to monthly variability. *Journal of Climate*, *2*(12), 1500–1506.

Hernandez, O., Jouanno, J., & Durand, F. (2016). Do the amazon and orinoco fresh-

water plumes really matter for hurricane-induced ocean surface cooling? *Journal of Geophysical Research: Oceans*, *121*(4), 2119–2141.

Hersbach, H., Bell, B., Berrisford, P., Hirahara, S., Horányi, A., Muñoz-Sabater, J., ... others (2020). The era5 global reanalysis. *Quarterly Journal of the Royal Meteorological Society*, *146*(730), 1999–2049.

Jochumsen, K., Rhein, M., Hüttl-Kabus, S., & Böning, C. W. (2010). On the propagation and decay of north brazil current rings. *Journal of Geophysical Research: Oceans*, *115*(C10).

Johns, W. E., Lee, T. N., Schott, F. A., Zantopp, R. J., & Evans, R. H. (1990). The north brazil current retroflection: Seasonal structure and eddy variability. *Journal of Geophysical Research: Oceans*, *95*(C12), 22103–22120.

Johns, W. E., Zantopp, R. J., & Goni, G. J. (2003). Cross-gyre transport by north brazil current rings. In *Elsevier oceanography series* (Vol. 68, pp. 411–441). Elsevier.

Karstensen, J., Lavik, G., Acquistapace, C., Baghen, G., Begler, C., Bendinger, A., ... others (2020). Eurec4a campaign, cruise no. msm89, 17. january-20. february 2020, bridgetown (barbados)-bridgetown (barbados), the ocean mesoscale component in the eurec4a++ field study.

Krishnamohan, K., Vialard, J., Lengaigne, M., Masson, S., Samson, G., Pous, S., ... Madec, G. (2019). Is there an effect of bay of bengal salinity on the northern indian ocean climatological rainfall? *Deep Sea Research Part II: Topical Studies in Oceanography*, *166*, 19–33.

Kwiatkowski, L., & Orr, J. C. (2018). Diverging seasonal extremes for ocean acidification during the twenty-first century. *Nature Climate Change*, *8*(2), 141–145.

Lange, D., Behrendt, A., & Wulfmeyer, V. (2019). Compact operational tropospheric water vapor and temperature raman lidar with turbulence resolution. *Geophysical Research Letters*, *46*(24), 14844–14853.

Laxenaire, R., Speich, S., Blanke, B., Chaigneau, A., Pegliasco, C., & Stegner, A. (2018). Anticyclonic eddies connecting the western boundaries of indian and atlantic oceans. *Journal of Geophysical Research: Oceans*, *123*(11), 7651–7677.

Leyba, I. M., Saraceno, M., & Solman, S. A. (2017). Air-sea heat fluxes associated to mesoscale eddies in the southwestern atlantic ocean and their dependence on different regional conditions. *Climate Dynamics*, *49*, 2491–2501.

L'Hégaret, P., Schütte, F., Speich, S., Reverdin, G., Baranowski, D. B., Czeschel, R., ... others (2022). Ocean cross-validated observations from the r/vs l'atalante, maria s. merian and meteor and related platforms as part of the eurec 4 a-oa/atomic campaign. *Earth System Science Data Discussions*, *2022*, 1–39.

Lindzen, R. S., & Nigam, S. (1987). On the role of sea surface temperature gradients in forcing low-level winds and convergence in the tropics. *Journal of Atmospheric Sciences*, *44*(17), 2418–2436.

Liu, H., Li, W., Chen, S., Fang, R., & Li, Z. (2018). Atmospheric response to mesoscale ocean eddies over the south china sea. *Advances in Atmospheric Sciences*, *35*, 1189–1204.

Liu, Y., Yu, L., & Chen, G. (2020). Characterization of sea surface temperature and air-sea heat flux anomalies associated with mesoscale eddies in the south china sea. *Journal of Geophysical Research: Oceans*, *125*(4), e2019JC015470.

Lloyd, S. (1982). Least squares quantization in pcm. *IEEE transactions on information theory*, *28*(2), 129–137.

Lukas, R., & Lindstrom, E. (1991). The mixed layer of the western equatorial pacific ocean. *Journal of Geophysical Research: Oceans*, *96*(S01), 3343–3357.

Ma, J., Xu, H., Dong, C., Lin, P., & Liu, Y. (2015). Atmospheric responses to oceanic eddies in the kuroshio extension region. *Journal of Geophysical Research: Atmospheres*, *120*(13), 6313–6330.

Ma, Z., Fei, J., Lin, Y., & Huang, X. (2020). Modulation of clouds and rain-

fall by tropical cyclone's cold wakes. *Geophysical Research Letters*, *47*(17), e2020GL088873.

Maes, C., & O'Kane, T. J. (2014). Seasonal variations of the upper ocean salinity stratification in the tropics. *Journal of Geophysical Research: Oceans*, *119*(3), 1706–1722.

Mahadevan, A., Jaeger, G. S., Freilich, M., Omand, M. M., Shroyer, E. L., & Sengupta, D. (2016). Freshwater in the bay of bengal: Its fate and role in air-sea heat exchange. *Oceanography*, *29*(2), 72–81.

Meissner, T., Wentz, F., Manaster, A., & Lindsley, R. (2019). Remote sensing systems smap ocean surface salinities level 3 running 8-day, version 4.0 validated release. *Remote Sensing Systems. Santa Rosa, CA, USA. Available online: www. remss. com/missions/smap/salinity/(accessed on 3 April 2021)*.

Merchant, C. J., Embury, O., Roberts-Jones, J., Fiedler, E., Bulgin, C. E., Corlett, G. K., ... others (2014). Sea surface temperature datasets for climate applications from phase 1 of the european space agency climate change initiative (sst cci). *Geoscience Data Journal*, *1*(2), 179–191.

Meroni, A. N., Parodi, A., & Pasquero, C. (2018). Role of sst patterns on surface wind modulation of a heavy midlatitude precipitation event. *Journal of Geophysical Research: Atmospheres*, *123*(17), 9081–9096.

Mignot, J., Lazar, A., & Lacarra, M. (2012). On the formation of barrier layers and associated vertical temperature inversions: A focus on the northwestern tropical atlantic. *Journal of Geophysical Research: Oceans*, *117*(C2).

Miller, J. R. (1976). The salinity effect in a mixed layer ocean model. *Journal of Physical Oceanography*, *6*(1), 29–35.

Minobe, S., Kuwano-Yoshida, A., Komori, N., Xie, S.-P., & Small, R. J. (2008). Influence of the gulf stream on the troposphere. *Nature*, *452*(7184), 206–209.

Mohr, W., Kinne, S., Baier, K., Baranowski, D., Chilinski, M., Gollop, J., ... L, W. (2020). *Eurec4a campaign, cruise no. m161, 17 jan 2020–3 mar 2020, bridgetown barbados–ponta delgada portugal.*

Neggers, R., Stevens, B., & Neelin, J. D. (2006). A simple equilibrium model for shallow-cumulus-topped mixed layers. *Theoretical and Computational Fluid Dynamics*, *20*, 305–322.

Olivier, L., Boutin, J., Reverdin, G., Lefèvre, N., Landschützer, P., Speich, S., ... others (2022). Wintertime process study of the north brazil current rings reveals the region as a larger sink for co 2 than expected. *Biogeosciences*, *19*(12), 2969–2988.

O'Neill, L. W., Chelton, D. B., Esbensen, S. K., & Wentz, F. J. (2005). High-resolution satellite measurements of the atmospheric boundary layer response to sst variations along the agulhas return current. *Journal of Climate*, *18*(14), 2706–2723.

Pailler, K., Bourles, B., & Gouriou, Y. (1999). The barrier layer in the western tropical atlantic ocean. *Geophysical Research Letters*, *26*(14), 2069–2072.

Pasquero, C., Desbiolles, F., & Meroni, A. N. (2021). Air-sea interactions in the cold wakes of tropical cyclones. *Geophysical Research Letters*, *48*(2), e2020GL091185.

Pearson, G., Davies, F., & Collier, C. (2009). An analysis of the performance of the ufam pulsed doppler lidar for observing the boundary layer. *Journal of Atmospheric and Oceanic Technology*, *26*(2), 240–250.

Peng, S., Yang, Q., Shupe, M. D., Xi, X., Han, B., Chen, D., ... Liu, C. (2023). The characteristics of atmospheric boundary layer height over the arctic ocean during mosaic. *Atmospheric Chemistry and Physics*, *23*(15), 8683–8703.

Quinn, P. K., Thompson, E. J., Coffman, D. J., Baidar, S., Bariteau, L., Bates, T. S., ... others (2021). Measurements from the rv ronald h. brown and related platforms as part of the atlantic tradewind ocean-atmosphere mesoscale interaction campaign (atomic). *Earth system science data*, *13*(4), 1759–1790.

Renault, L., Masson, S., Oerder, V., Jullien, S., & Colas, F. (2019). Disentangling the mesoscale ocean-atmosphere interactions. *Journal of Geophysical Research: Oceans*, *124*(3), 2164–2178.

Renault, L., Molemaker, M. J., McWilliams, J. C., Shchepetkin, A. F., Lemarié, F., Chelton, D., ... Hall, A. (2016). Modulation of wind work by oceanic current interaction with the atmosphere. *Journal of Physical Oceanography*, *46*(6), 1685–1704.

Reverdin, G., Olivier, L., Foltz, G., Speich, S., Karstensen, J., Horstmann, J., ... others (2021). Formation and evolution of a freshwater plume in the northwestern tropical atlantic in february 2020. *Journal of Geophysical Research: Oceans*, *126*(4), e2020JC016981.

Richardson, P., Hufford, G., Limeburner, R., & Brown, W. (1994). North brazil current retroflection eddies. *Journal of Geophysical Research: Oceans*, *99*(C3), 5081–5093.

Roberts, J. B., Clayson, C. A., Robertson, F. R., & Jackson, D. L. (2010). Predicting near-surface atmospheric variables from special sensor microwave/imager using neural networks with a first-guess approach. *Journal of Geophysical Research: Atmospheres*, *115*(D19).

Seidel, D. J., Zhang, Y., Beljaars, A., Golaz, J.-C., Jacobson, A. R., & Medeiros, B. (2012). Climatology of the planetary boundary layer over the continental united states and europe. *Journal of Geophysical Research: Atmospheres*, *117*(D17).

Shao, M., Ortiz-Suslow, D. G., Haus, B. K., Lund, B., Williams, N. J., Özgökmen, T. M., ... Klymak, J. M. (2019). The variability of winds and fluxes observed near submesoscale fronts. *Journal of Geophysical Research: Oceans*, *124*(11), 7756–7780.

Smith, W. H., & Sandwell, D. T. (1997). Global sea floor topography from satellite altimetry and ship depth soundings. *Science*, *277*(5334), 1956–1962.

Speich, S. (2021). *The embarked science team: Eurec4a-oa. cruise report. 19 january–19 february 2020. vessel: L'atalante.* Ifremer: Brest, France.

Sprintall, J., & Tomczak, M. (1992). Evidence of the barrier layer in the surface layer of the tropics. *Journal of Geophysical Research: Oceans*, *97*(C5), 7305–7316.

Stephan, C. C., Schnitt, S., Schulz, H., Bellenger, H., De Szoeke, S. P., Acquistapace, C., ... others (2021). Ship-and island-based atmospheric soundings from the 2020 eurec¡ sup¿ 4¡/sup¿ a field campaign. *Earth System Science Data*, *13*(2), 491–514.

Stevens, B., Bony, S., Farrell, D., Ament, F., Blyth, A., Fairall, C., ... others (2021). Eurec 4 a. *Earth System Science Data Discussions*, *2021*, 1–78.

Subirade, C., L'Hégaret, P., Speich, S., Laxenaire, R., Karstensen, J., & Carton, X. (2023). Combining an eddy detection algorithm with in-situ measurements to study north brazil current rings. *Remote Sensing*, *15*(7), 1897.

Takatama, K., & Schneider, N. (2017). The role of back pressure in the atmospheric response to surface stress induced by the kuroshio. *Journal of the Atmospheric Sciences*, *74*(2), 597–615.

Tanimoto, Y., Nakamura, H., Kagimoto, T., & Yamane, S. (2003). An active role of extratropical sea surface temperature anomalies in determining anomalous turbulent heat flux. *Journal of Geophysical Research: Oceans*, *108*(C10).

Vautard, R., & Ghil, M. (1989). Singular spectrum analysis in nonlinear dynamics, with applications to paleoclimatic time series. *Physica D: Nonlinear Phenomena*, *35*(3), 395–424.

Vautard, R., Yiou, P., & Ghil, M. (1992). Singular-spectrum analysis: A toolkit for short, noisy chaotic signals. *Physica D: Nonlinear Phenomena*, *58*(1-4), 95–126.

Vialard, J., & Delecluse, P. (1998). An ogcm study for the toga decade. part i: Role

of salinity in the physics of the western pacific fresh pool. *Journal of Physical Oceanography*, *28*(6), 1071–1088.

Villas Bôas, A., Sato, O., Chaigneau, A., & Castelão, G. (2015). The signature of mesoscale eddies on the air-sea turbulent heat fluxes in the south atlantic ocean. *Geophysical Research Letters*, *42*(6), 1856–1862.

Vogelezang, D., & Holtslag, A. (1996). Evaluation and model impacts of alternative boundary-layer height formulations. *Boundary-Layer Meteorology*, *81*(3-4), 245–269.

Wallace, J. M., Mitchell, T., & Deser, C. (1989). The influence of sea-surface temperature on surface wind in the eastern equatorial pacific: Seasonal and interannual variability. *Journal of Climate*, *2*(12), 1492–1499.

Wang, Z., & Sassen, K. (2001). Cloud type and macrophysical property retrieval using multiple remote sensors. *Journal of Applied Meteorology and Climatology*, *40*(10), 1665–1682.

Weller, R., & Anderson, S. (1996). Surface meteorology and air-sea fluxes in the western equatorial pacific warm pool during the toga coupled ocean-atmosphere response experiment. *Journal of Climate*, *9*(8), 1959–1990.

Xu, H., Xu, M., Xie, S.-P., & Wang, Y. (2011). Deep atmospheric response to the spring kuroshio over the east china sea. *Journal of Climate*, *24*(18), 4959–4972.

Yang, H., Liu, J., Lohmann, G., Shi, X., Hu, Y., & Chen, X. (2016). Ocean-atmosphere dynamics changes associated with prominent ocean surface turbulent heat fluxes trends during 1958–2013. *Ocean Dynamics*, *66*, 353–365.

Zhang, D., Cronin, M. F., Meinig, C., Farrar, J. T., Jenkins, R., Peacock, D., ... Yang, Q. (2019). Comparing air-sea flux measurements from a new unmanned surface vehicle and proven platforms during the spurs-2 field campaign. *Oceanography*, *32*, 122 - 133. Retrieved from `https://doi.org/10.5670/oceanog.2019.220`

Zheng, Y. (2019). Theoretical understanding of the linear relationship between convective updrafts and cloud-base height for shallow cumulus clouds. part i: Maritime conditions. *Journal of the Atmospheric Sciences*, *76*(8), 2539–2558.

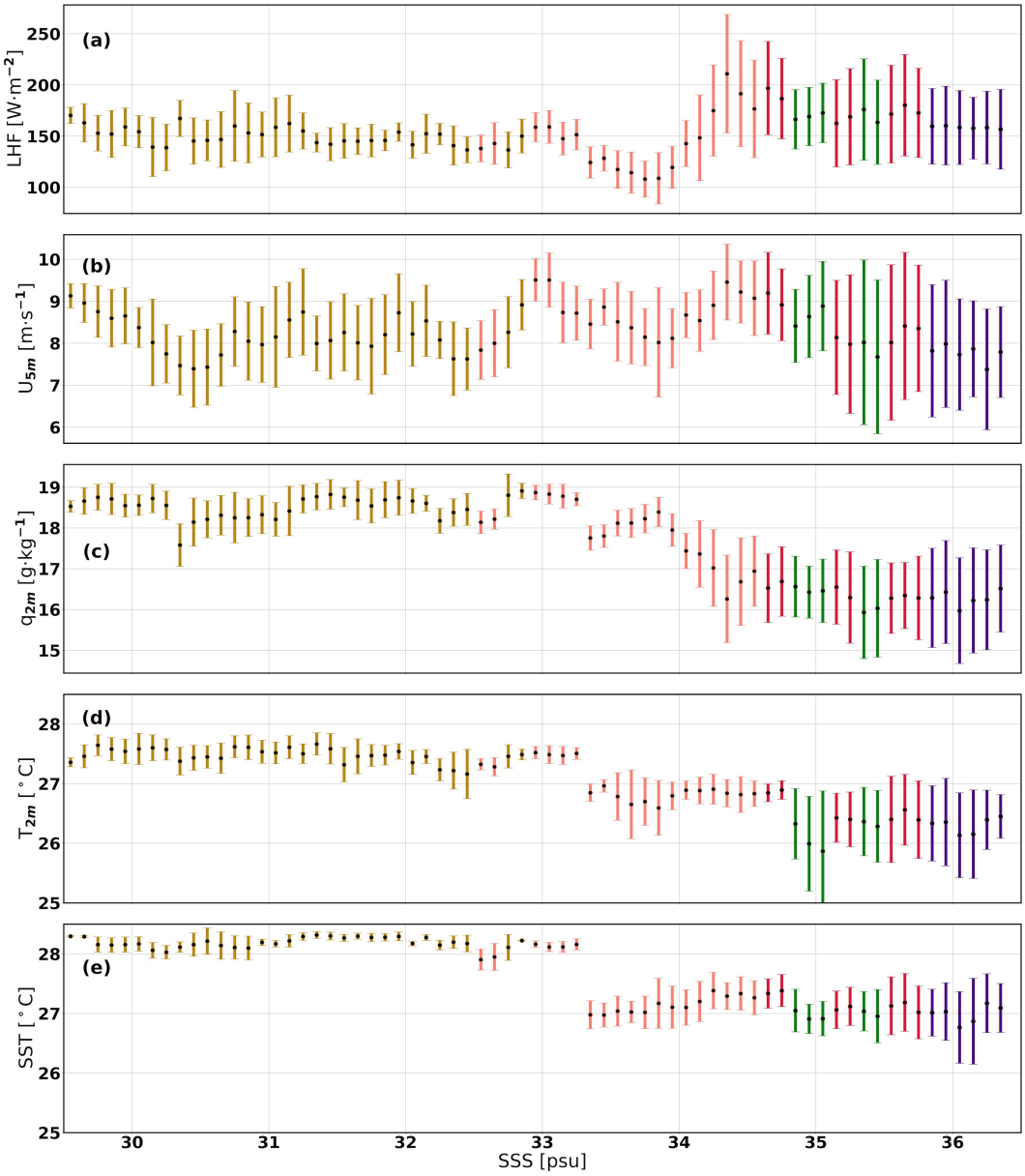

Figure 4. Binning in SSS 0.1 psu intervals of (a) LHF computed with COARE3.5, (b) U_{5m}, (c) q_{2m}, (d) T_{2m}, and (e) SST. The dots indicate the mean values in the interval and the error bars indicate the standard deviation. The error bars are color-coded with the water mass mode on each interval. Data are considered between 13^{th} January and 11^{th} April 2020.

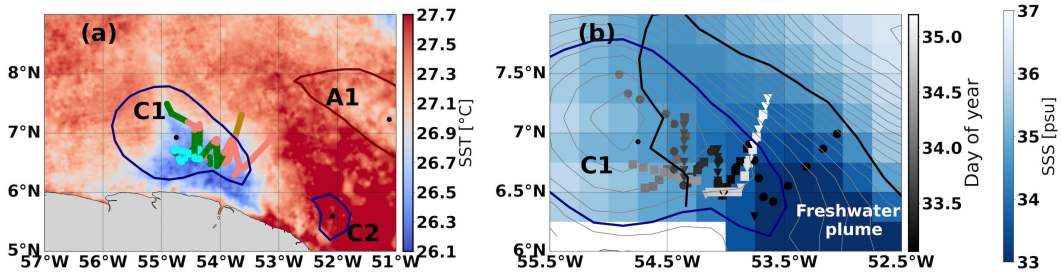

Figure 5. (a) Tracks of the various instruments sampling the SSS-SST front between the 2^{nd} and the 5^{th} of February 2020, color-coded with the water masses they cross. The background shading indicates the mean MUR-JPL SST between the 2^{nd} and the 5^{th}. (b) Zoom in on the tracks of the different instruments sampling the SSS-SST front, color-coded with the day of the year when each measurement was made. Squares represent the *Atalante* MVP, dots the ARTHUS/DLs vertical profiles, and inverted triangles the *Atalante* meteorological mast air-sea interface sites. The background shading indicates the mean SSS between 2^{nd} and 5^{th} February 2020, and the black contour the mean 34.7 psu isoline chosen to delineate the Amazon plume. These last two features are obtained with the RS SMAP L3 SSS dataset. The light gray contours represent the ADT isolines. In both panels, cyclonic (anticyclonic) eddies detected with TOEddies (Laxenaire et al., 2018) are represented by the closed blue (red) contours.

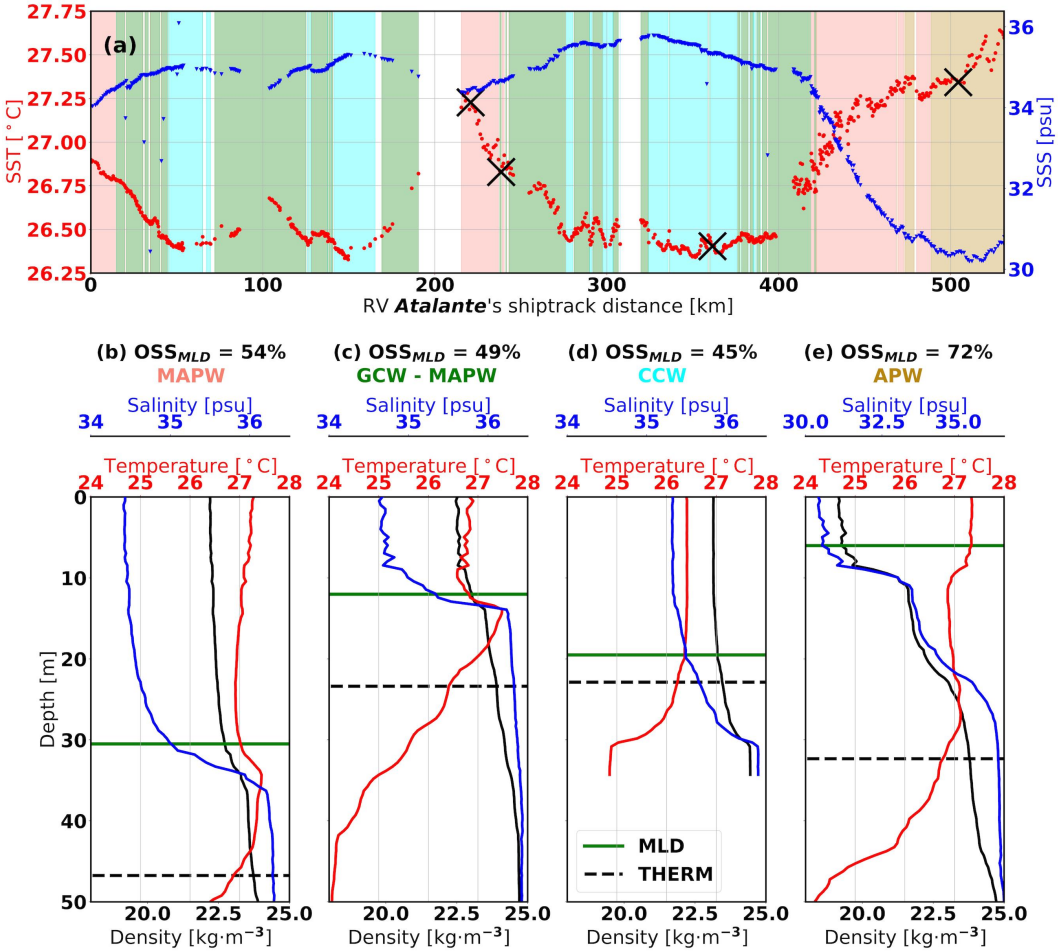

Figure 6. (a) RV *Atalante* TSG SST (red) and SSS (blue) time series between 2^{nd} and 5^{th} February 2020. The shading indicates the sampled water mass. The crosses mark the locations of the vertical profiles shown in panels (b), (c), (d), and (e), in the same order from left to right. Density is shown in black, temperature in red and salinity in blue. The MLD is shown as a solid green line and THERM as a dashed black line.

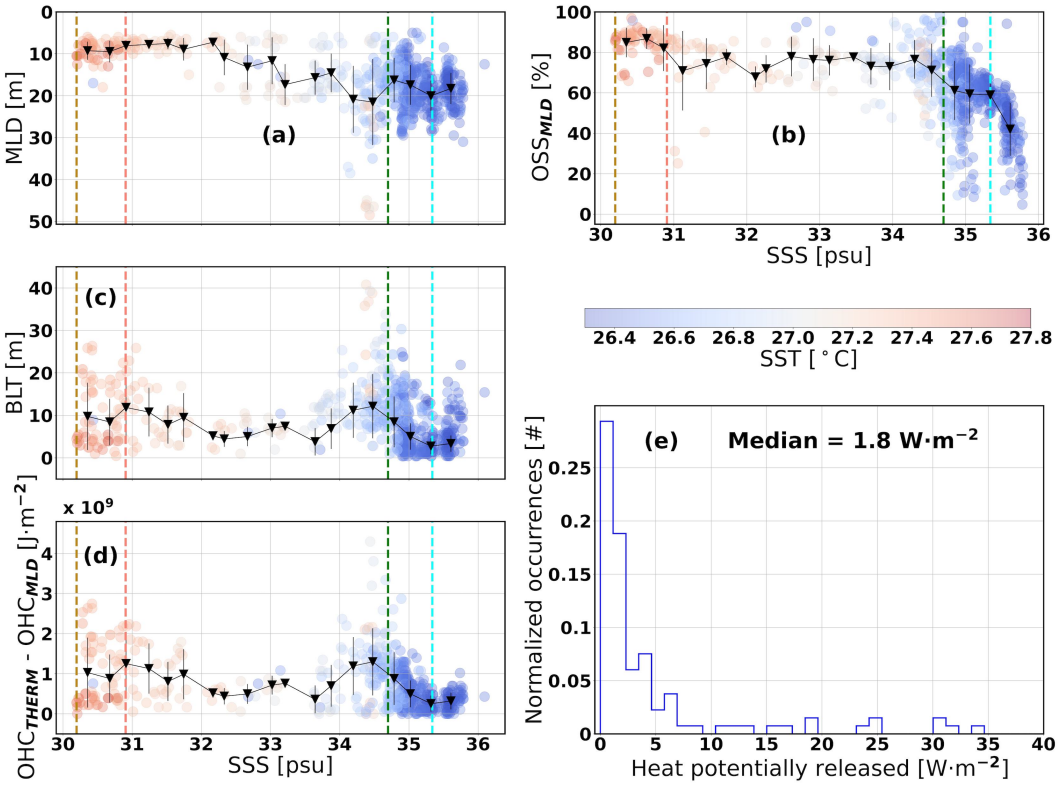

Figure 7. SSS binning of (a) mixed layer depth (MLD), (b) OSS_{MLD} index, (c) barrier layer thickness (BLT) computed as the difference between THERM and MLD, (d) ocean heat content per unit of area stored between THERM and the mixed layer depth. Colors indicate SST, and black lines, inverted triangles, and error bars indicate means and standard deviations within the 20 equal-width bins across the full salinity range. The colored dashed vertical lines indicate the freshest boundaries between clusters in the binning (color-coded with water mass as in Fig. 2). (e) shows the probability density function (PDF) of the heat potentially released to the atmosphere according to eq. 11 in waters between 34 and 35 psu.

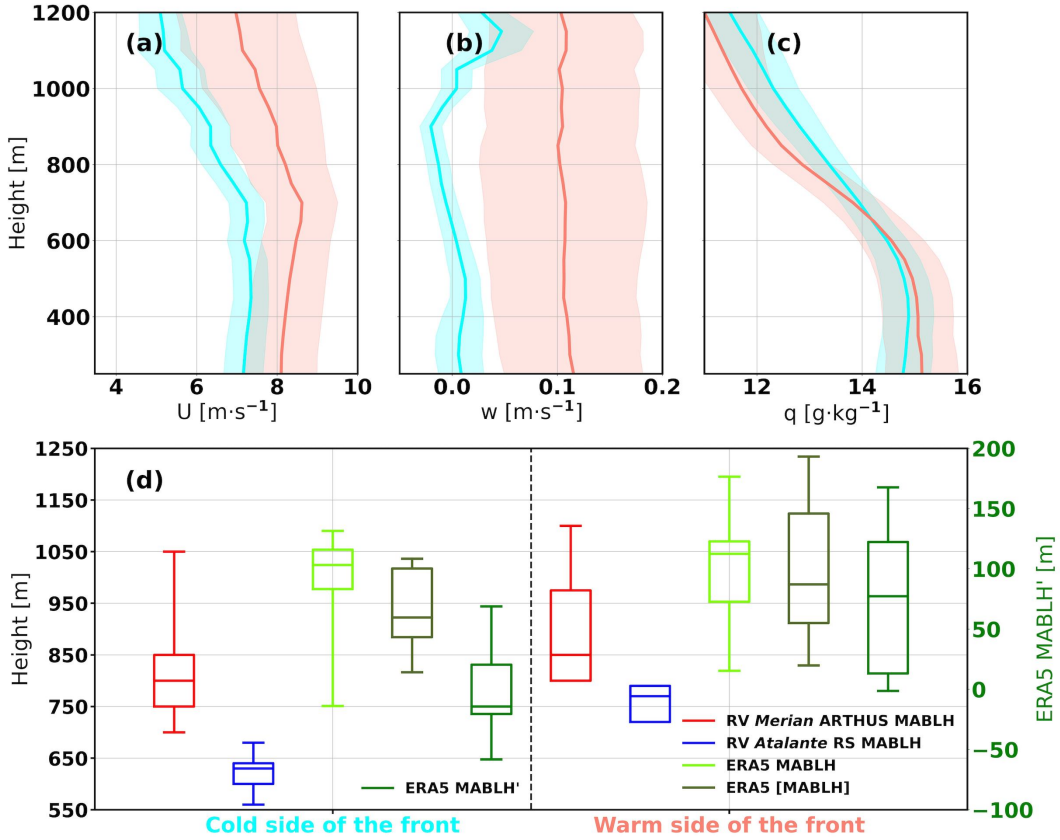

Figure 8. Averaged vertical profiles from the RV *Merian* ARTHUS/DL of (a) horizontal wind speed, (b) vertical wind speed, (c) specific humidity for the 25% lowest *Merian* TSG SSTs (cyan, color-coded with the mode cluster) and for the 25% highest *Merian* TSG SSTs (salmon, color coded with the mode cluster). Solid lines represent means and shading represents standard deviations. (d) Box plots of the MABLH calculated from the *Merian* ARTHUS (red), *Atalante* RS (blue), and collocated ERA5 data (lime green). The olive green box plots represent ERA5 [MABLH] and the green box plots represent MABLH'. The five left box plots correspond to the coldest SST values and the remaining five are computed over the warmest SST values. To maximize the number of observations per boxplot and since the SST values vary between data sets, here we choose the warm (cold) side of the front to be the warmest (coldest) most sampled water mass.

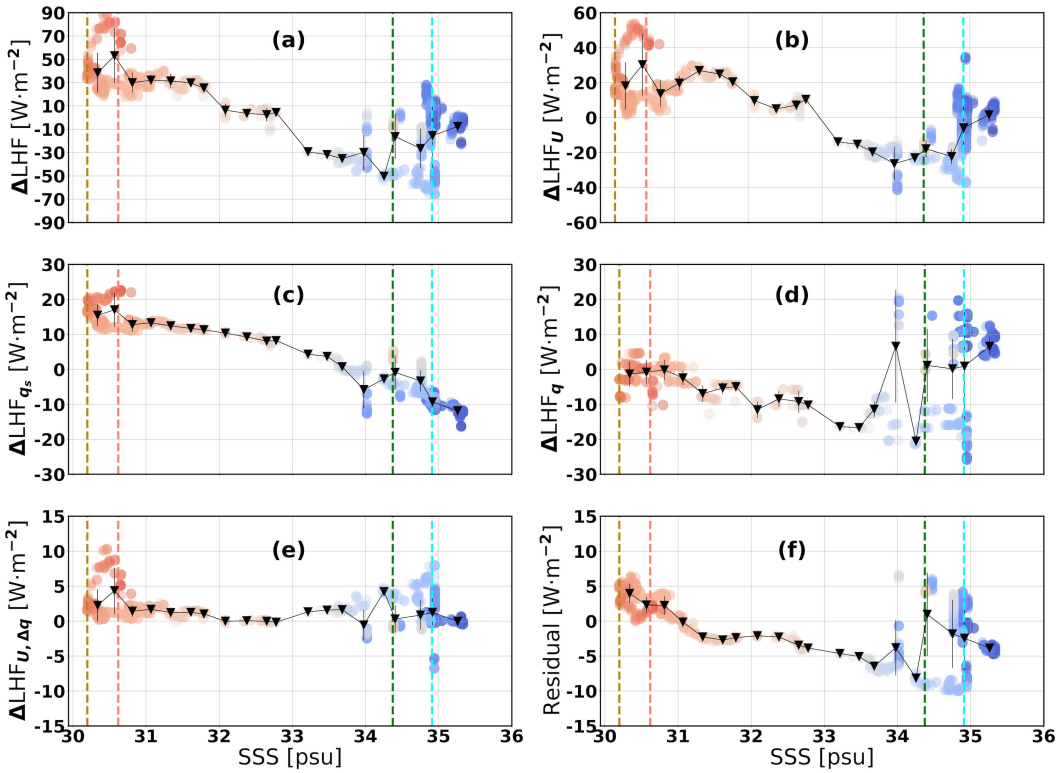

Figure 9. SSS binning of the various terms in eq. 12 (a) ΔLHF, (b) ΔLHF_U, (c) ΔLHF_{q_s}, (d) ΔLHF_q, (e) $\Delta\text{LHF}_{U,\Delta q}$, and (f) residual. As in Fig. 7, the colors in the markers denote *Atalante* TSG SST values, and the black lines and error bars denote means and standard deviations within 20 bins over the full salinity range. The vertical dashed lines represent the freshest salinity boundaries between the four clusters.

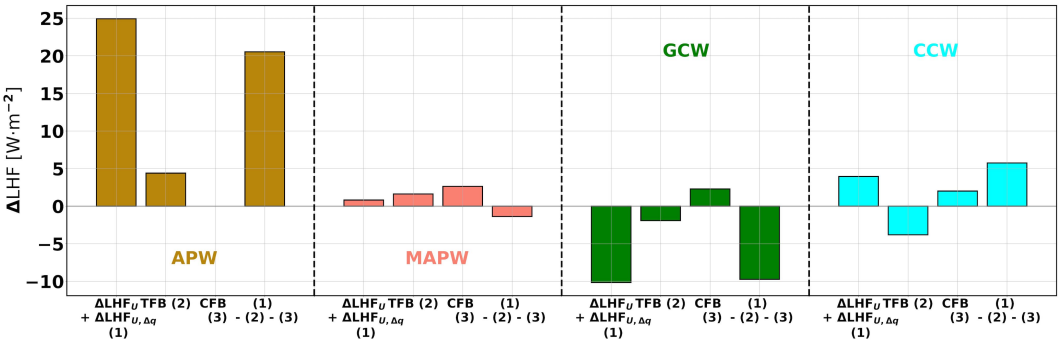

Figure 10. TFB and CFB evaluation in the four water masses. In each bar quartet, from left to right, the bars represent $\Delta\text{LHF}_U + \Delta\text{LHF}_{U,\Delta q}$, the LHF change as a consequence of the TFB, the LHF change associated with the CFB, and the difference between the first and the sum of the second and third. Same color code as in Fig. 2.

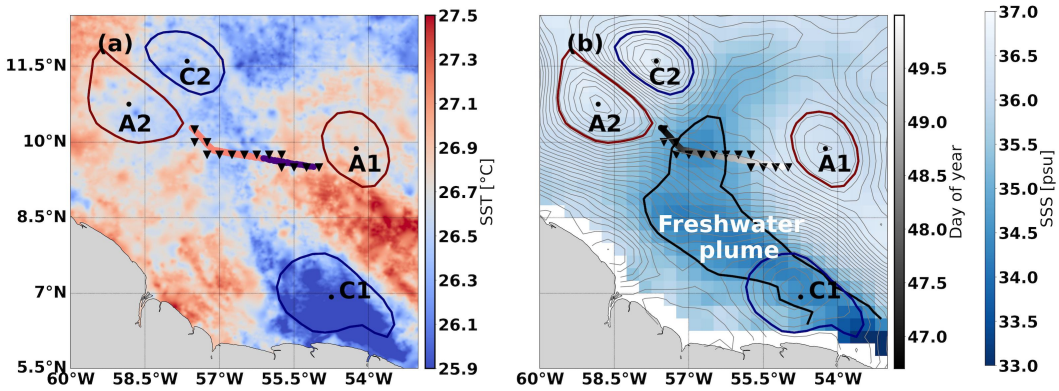

Figure 11. (a) Track of SD1063 sampling the SSS-SST front between 16^{th} and 19^{th} February 2020, color-coded with the water masses it crosses. The background shading indicates the mean MUR-JPL SST between the same dates. (b) Track of SD1063 color-coded with the time of each measurement. The gray contours correspond to the ADT isolines, and the thick black contour delimits the freshwater plume defined by the 34.7 psu isoline. The background shading indicates the mean RS SMAP L3 SSS between 16^{th} and 19^{th} February 2020. In both panels, cyclonic eddies are represented by thick blue contours and anticyclonic eddies by thick red contours, and the triangles represent the collocated ERA5 data. Mesoscale eddies are detected with TOEddies (Laxenaire et al., 2018).

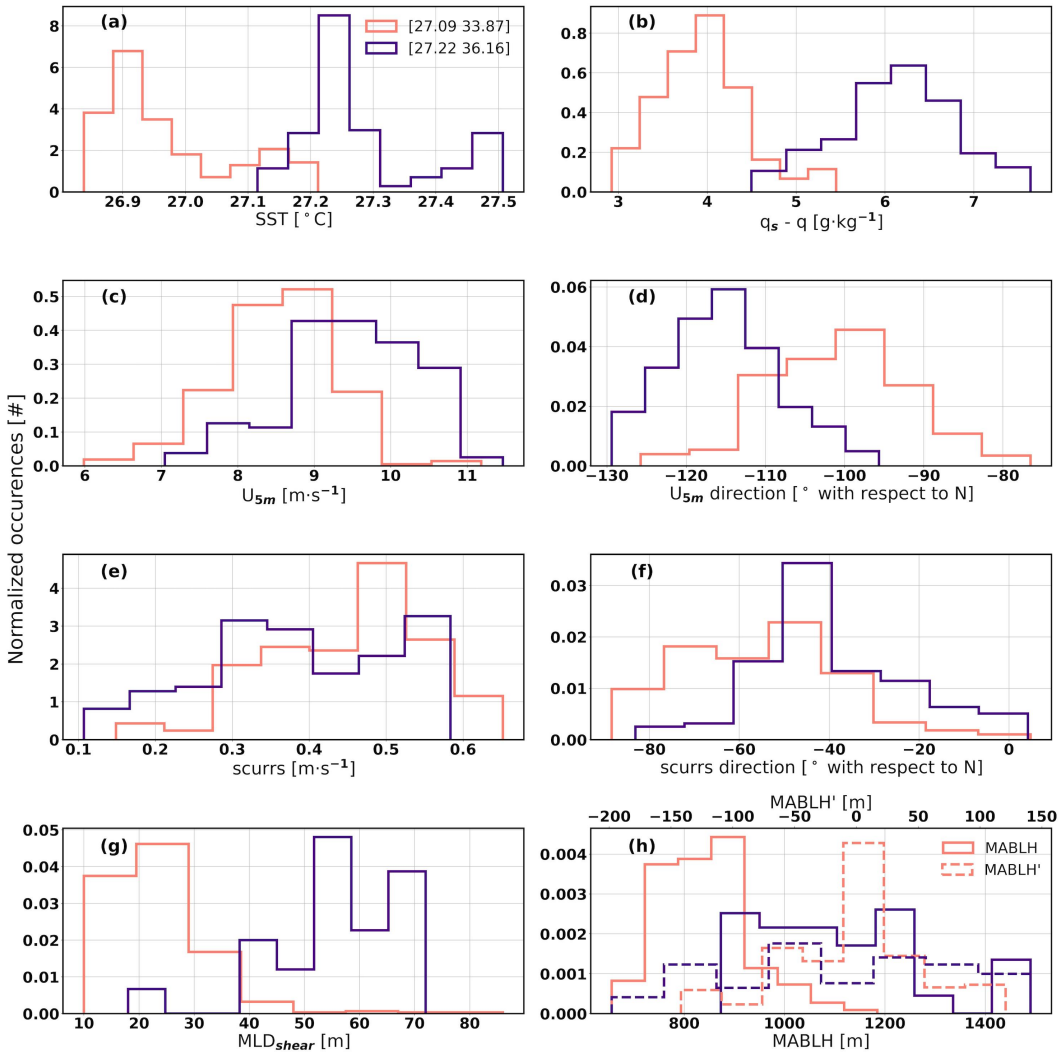

Figure 12. Histograms of the various Saildrone air-sea variables. (a) SST; (b) specific humidity deficit, defined as the difference between saturation specific humidity (computed as in Buck (1981)) and $q_{2.3m}$; (c) 5.2 m wind speed and (d) 5.2 m wind direction; (e) surface current norm and (f) surface current direction; (g) MLD computed from the shear maximum (MLD_{shear}); (h) collocated ERA5 MABLH (solid) and MABLH' (dashed). The probability density functions (PDFs) in all panels are color-coded with the cluster to which they belong. The [SST-SSS] centroids of each cluster are shown in the legend of (a). Data were collected between 16^{th} and 19^{th} of February 2020.

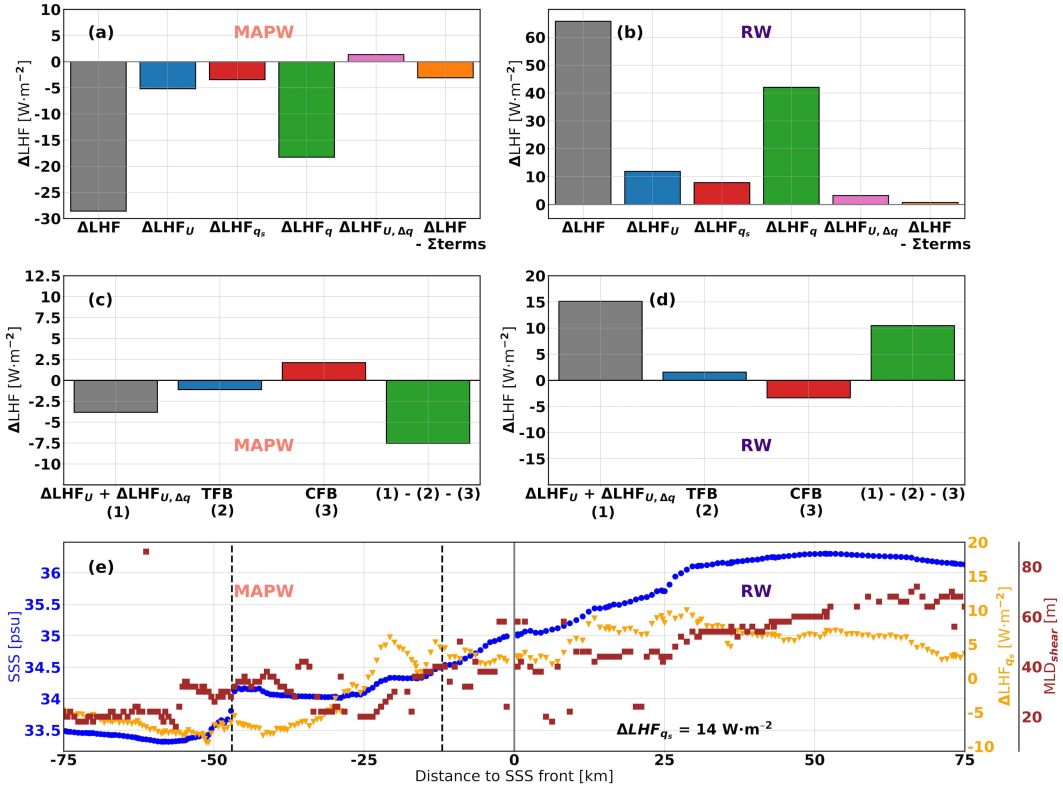

Figure 13. (a) and (b) show the LHF decomposition for the MAPWs and RWs, respectively. The bars in each plot represent from left to right: ΔLHF, ΔLHF_u, ΔLHF_{q_s}, ΔLHF_q, $\Delta\text{LHF}_{U,\Delta q}$, and residual. (c) and (d) depict from left to right the decomposition of the total wind speed contribution to the LHF change ($\Delta\text{LHF}_U + \Delta\text{LHF}_{U,\Delta q}$), the TFB contribution, the CFB contribution, and the background contribution. (e) Time series of SSS (blue), ΔLHF_{q_s} (yellow), and MLD_{shear} (brown) across the SSS front (defined as the location where the water mass changes). Data were acquired between 16^{th} and 19^{th} February 2020.

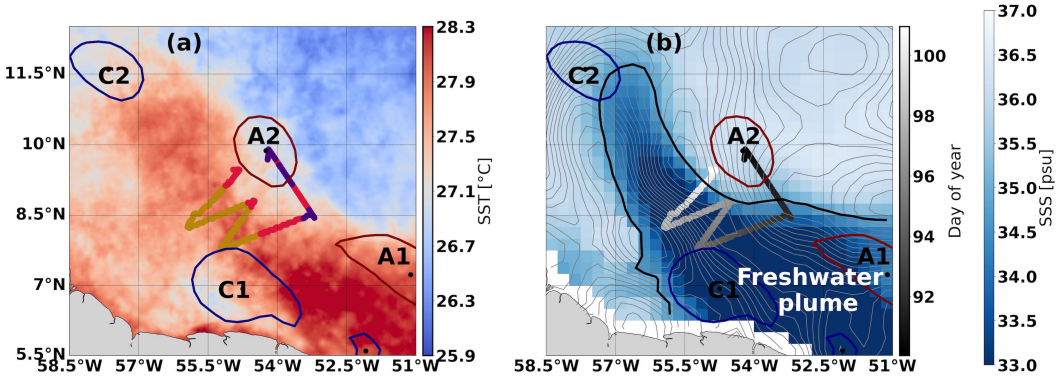

Figure 14. (a) Track of SD1064 sampling the freshwater plume front between 31^{st} March and 11^{th} April 2020, color-coded with the water masses it crosses. The background shading indicates the mean MUR-JPL SST between the same dates. (b) Track of SD1064 color-coded with the time of each measurement. The gray contours correspond to the ADT isolines, and the thick black contour delineates the freshwater plume defined by the 34.7 psu isoline. The background shading indicates the mean RS SMAP L3 SSS between 31^{st} March and 11^{th} April 2020. In both panels, cyclonic eddies are represented by thick blue contours and anticyclonic eddies by thick red contours. Mesoscale eddies are detected with TOEddies (Laxenaire et al., 2018).

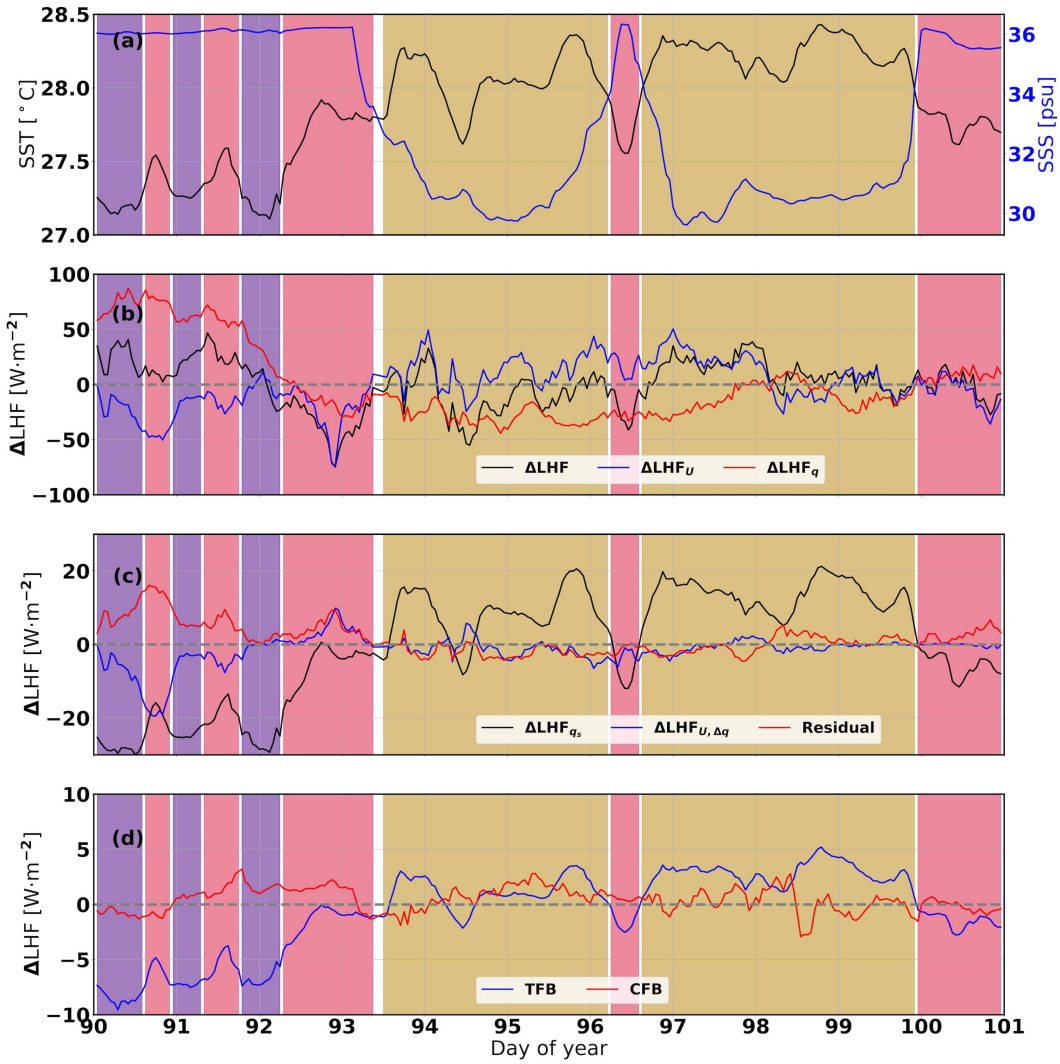

Figure 15. Time series along the SD1064 track of (a) TSG SST (black), SSS (blue); (b) ΔLHF (black), ΔLHF_U (blue) and ΔLHF_q (red); (c) ΔLHF_{q_s} (black), $\Delta\text{LHF}_{U,\Delta q}$ (blue) and residual (red); (d) TFB (blue) and CFB (red). The background color indicates the crossed water mass (see definition in Fig. 2.

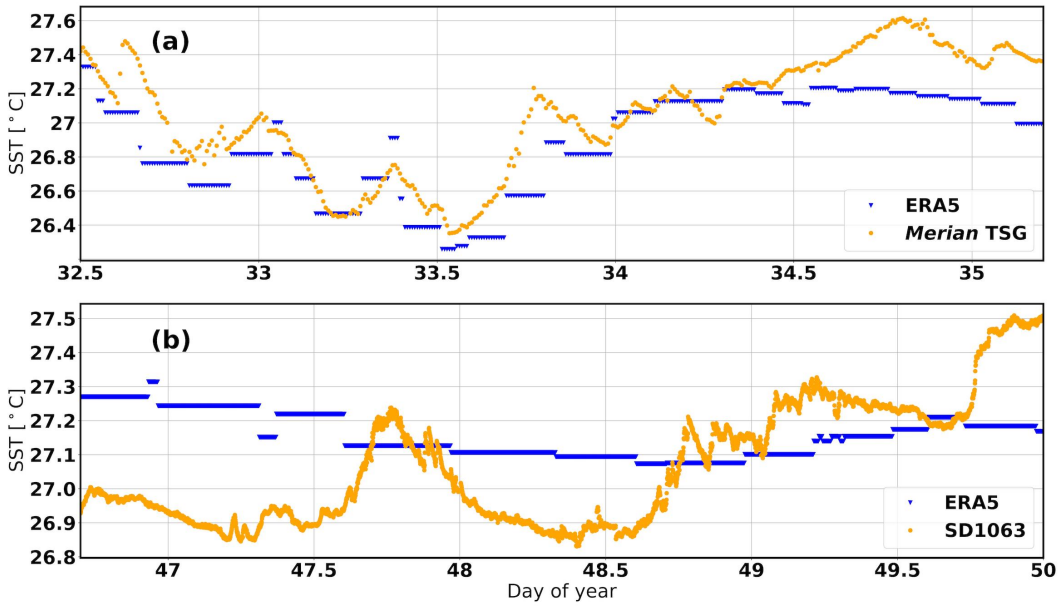

Figure 16. Comparison between the collocated ERA5 SSTs (blue) and (a) the *Merian* TSG SST between the 2^{nd} and the 5^{th} of February 2020 and (b) the SD1063 TSG SST between the 16^{th} and the 19^{th} of February 2020.

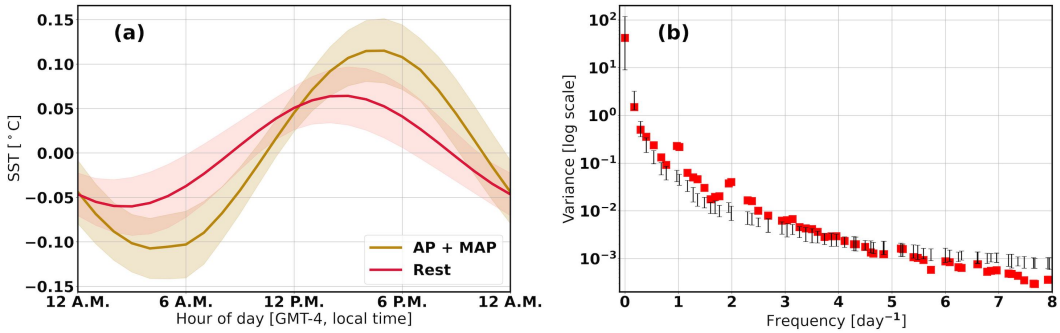

Figure 17. (a) SD1064 SST mean diurnal cycle (solid lines) of the APWs and MAPWs (golden) and the rest of the clusters (crimson) and the corresponding standard deviation (shading). (b) Variance associated to the different PCs of the SD1064 SST time series as a function of their dominant frequency (red squares). The errorbars denote the 5% and the 95% percentiles of the each PC's variance distribution after repeating the SSA 5000 times assuming the PCs are generated with an AR(1) process.

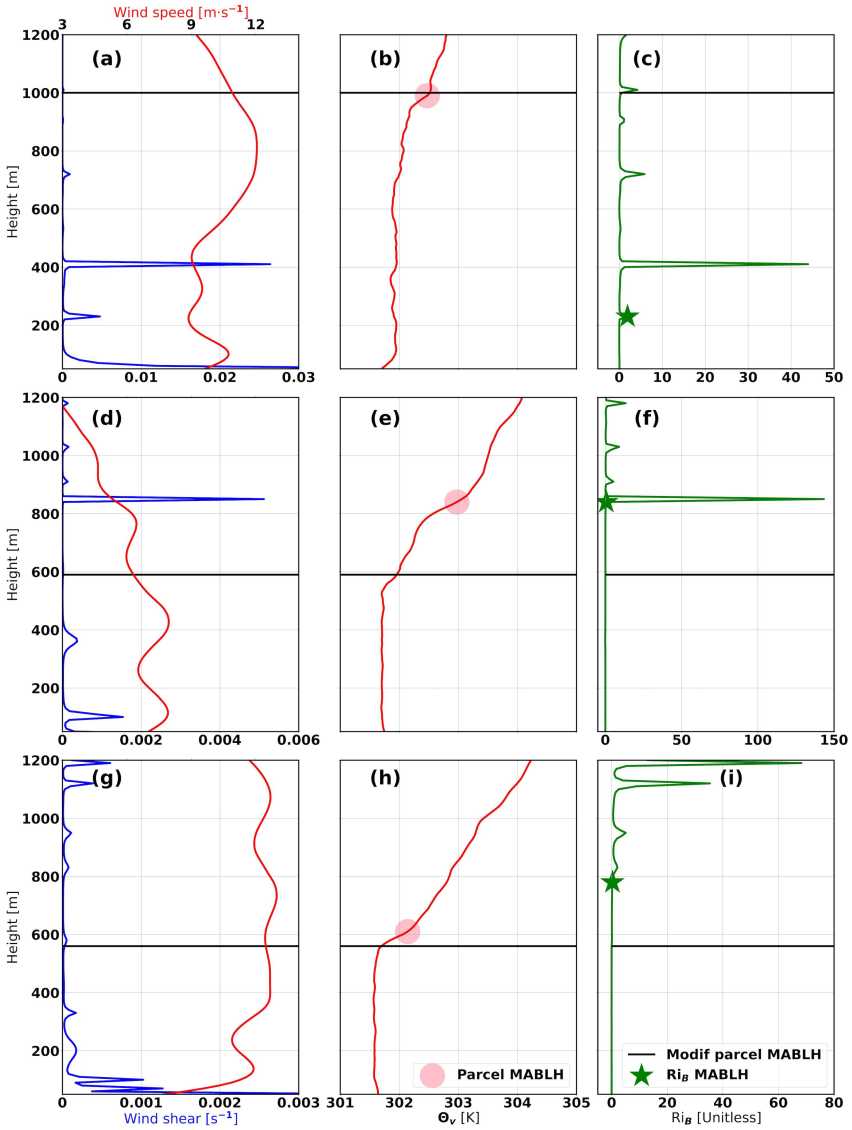

Figure 18. (a), (d) and (g) contain wind shear (blue) and wind speed (red) RS vertical profiles. (b), (e) and (h) depict θ_v vertical profiles (pink line) and the MABLH values from the gradient (parcel) method (pink circles). (c), (f) and (i) show Ri_B vertical profiles (green) and the MABLH computed using the Ri_B method (green stars). In all the panels, the horizontal black line represents the MABLH calculated with the modified parcel method. Each panel row corresponds to a different location.

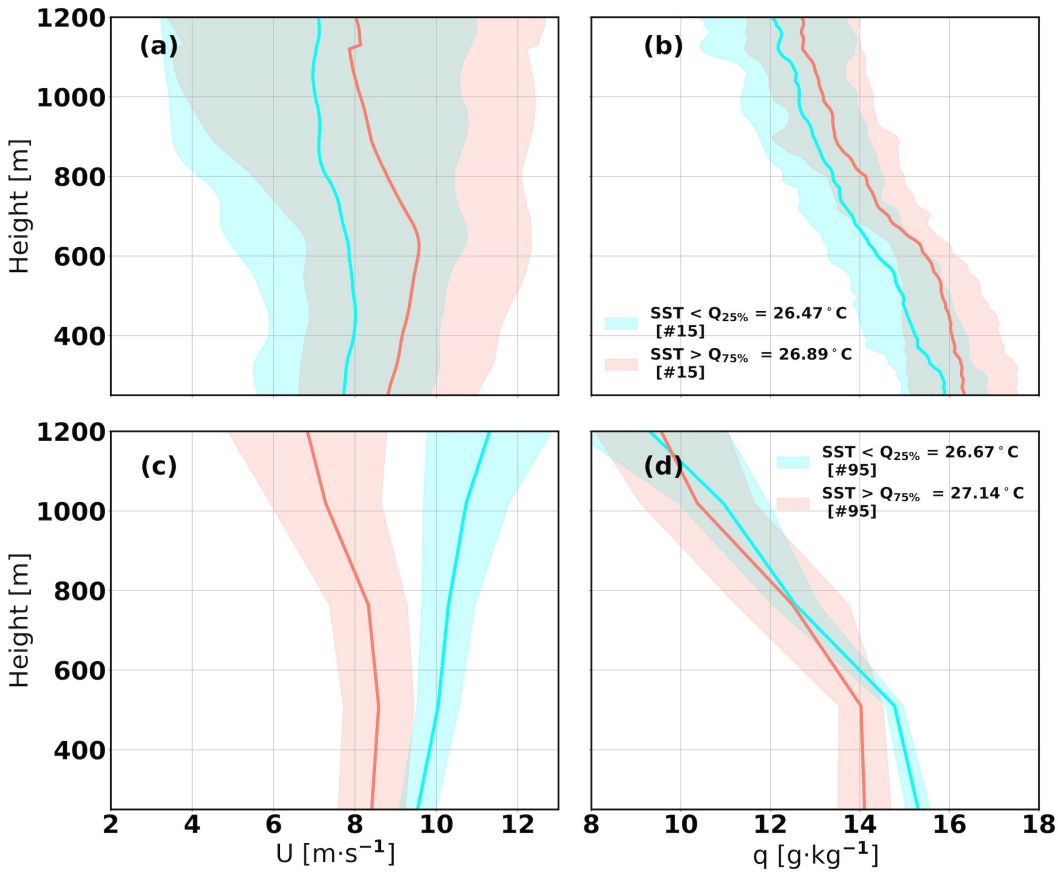

Figure 19. Mean vertical profiles (solid lines) and standard deviations (shading) of (a) *Atalante* RS horizontal wind speed, (b) RS specific humidity, (c) ERA5 collocated horizontal wind speed and (d) ERA5 collocated specific humidity. Like in Fig. 8, the profiles are obtained from the warmest and coldest SST 25% percentiles and are color-coded according to their mode cluster.

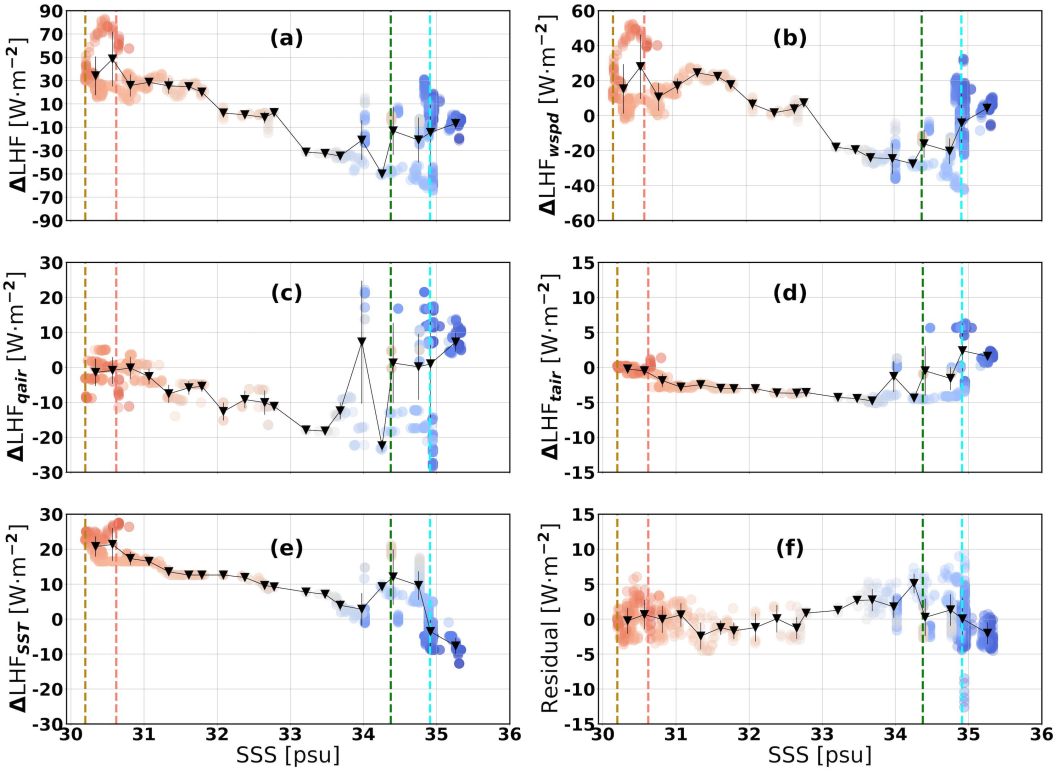

Figure 20. As in Fig. 9 but for the numerical Taylor deconvolution. (a) represents the total change in ΔLHF, (b) ΔLHF_{wspd}, (c) ΔLHF_{q}, (d) ΔLHF_{T}, (e) ΔLHF_{SST} and (f) Residual